



Article

Mineral Paragenesis Precipitating in Salt Flat Pools of Continental Environments Replicated in Microbial Mat Microcosms without Evaporation

Óscar Cabestrero ^{1,*}, Cinthya Tebes-Cayo ^{1,*}, Nancy W. Hinman ² and Cecilia Demergasso ^{1,*}

¹ Centro de Biotecnología 'Profesor Alberto Ruiz', Universidad Católica del Norte, Angamos 0610, Antofagasta 1270709, Chile

² Department of Geosciences, University of Montana, Charles H Clapp Building Rm 126, 32 Campus Dr, Missoula, MT 59812, USA; nancy.hinman@umontana.edu

* Correspondence: oscar.cabestrero@ucn.cl (Ó.C.); ctebes@ucn.cl (C.T.-C.); cdemerga@ucn.cl (C.D.)

Abstract: Mineral precipitation can be observed in natural environments, such as lagoons, rivers, springs, and soils. The primary precipitation process has long been believed to be abiotic due to evaporation, leading to phase supersaturation. However, biotic interactions of microbial metabolism, organic compounds, and dissolved ions leading to mineral precipitation has been shown in laboratory studies using single-organism culture. The increase in pH inducing calcium carbonate precipitation due to oxygenic photosynthesis by *Cyanobacteria* and the release of ions due to organic matter decomposition by *Firmicutes*-inducing magnesium carbonate precipitation are recognized examples. As microbes do not live as pure cultures in natural environments but form complex communities, such pure culture lab studies do not reflect natural conditions. In this study, we grew natural complex microbial communities in microcosm conditions using filtered brine as water column and two types of natural gypsum substrates, and we replenished incubations to avoid evaporation. We monitored microbial communities through optical microscopy and analyzed mineral paragenesis in association with and without microbes, using different analytical techniques, such X-ray diffraction, and optical and field emission scanning electron microscopies. To detect changes throughout the experiment, small amounts of water column brine were extracted for physicochemical determinations. We were able to detect mineral paragenesis, avoiding evaporation, including major phases of chemical sedimentary rocks, such as gypsum, calcium carbonate, and some silicates in association to microbes. In addition, we evidenced that the use of natural substrates positively impacts growth of microbial communities, promoting the development of more biomass. This study can be seen as the first attempt and proof of concept of differentiating biotic and abiotic participation in evaporitic deposits, as they can form mineral paragenesis without evaporation. Future studies with microcosm experiments using microbial mats will be needed to establish mineral precipitation induced by micro-organisms and their extracellular polymeric substances (EPS), specifically to replicate mineral paragenesis sedimented from natural brines.

Keywords: microcosms; microbial mats; entire communities; minerals; precipitation; no evaporation



Citation: Cabestrero, Ó.; Tebes-Cayo, C.; Hinman, N.W.; Demergasso, C. Mineral Paragenesis Precipitating in Salt Flat Pools of Continental Environments Replicated in Microbial Mat Microcosms without Evaporation. *Minerals* **2022**, *12*, 646. <https://doi.org/10.3390/min12050646>

Academic Editors: Oluwatoosin Agbaje, Olev Vinn and Yul Roh

Received: 13 January 2022

Accepted: 13 May 2022

Published: 20 May 2022

Publisher's Note: MDPI stays neutral with regard to jurisdictional claims in published maps and institutional affiliations.



Copyright: © 2022 by the authors. Licensee MDPI, Basel, Switzerland. This article is an open access article distributed under the terms and conditions of the Creative Commons Attribution (CC BY) license (<https://creativecommons.org/licenses/by/4.0/>).

1. Introduction

Saline playa lakes and salars are continental environments scattered worldwide in which mineral precipitation can be observed. Eugster and Hardie [1] proposed that the initial chemical composition of the evaporating brine controls the sequence of mineral crystallization that follows three major pathways in continental environments. Decades ago, most geochemists agreed with this model, and it has been improved and completed since then [2]. More recently, researchers thought that each geochemical case needed to be evaluated individually because brines and sediments contain microbes that can interact with the environment, changing the saturation state of phases and affecting mineral

precipitation [3]. As the classical geochemical model of Eugster and Hardie [1] has not been proven to work perfectly in the presence of organisms, its validity should be limited to abiotic (or near-abiotic) environmental scenarios. These abiotic environments seem scarce in nature, as it is difficult to find natural environments on Earth where organisms do not occur and thrive [4]. We now know that microbes influence the formation of minerals and have affected global biogeochemical cycles since the appearance of life on Earth [5]. Montague [6] stated, “*The physical and chemical properties of sediments that contain a significant biotic community are radically different from those of abiotic sediments*”. Indeed, micro-organisms may play a pivotal role in the physical and chemical environmental processes associated with mineral precipitation (e.g., [7]). It is especially expected in extreme environments that may have been extensive on Early Earth and persist today in specific places [8].

These extreme hypersaline evaporitic environments are colonized by micro-organisms, often occurring as microbial mats, which are responsible for the formation of microbialites, i.e., organosedimentary deposits accreted by a complex interplay between the environment and benthic microbial communities that trap and bind detrital sediments and/or serve as loci for mineral precipitation [9]. Present-day examples of subaqueous gypsum/halite-dominated microbialites are found in hypersaline environments around the globe, for instance, the Netherlands Antilles [10], Mexico [11], Venezuela [12], Egypt [13], Qatar [14], and Spain [15–19], among others. Exceptionally numerous deposits of microbialites of these types can be found in the vicinity of the Andes Mountains (e.g., [20–23]).

Many studies in these areas and other related extreme environments have isolated microbes to elucidate microbial–mineral interactions. Most have focused on the role of specific bio-organic components (e.g., organic molecules of organelles, organelles of cells, or cells of organisms) in mineral precipitation by using traditional biological methods, such as cultures, bacterial isolates, and enrichments ([24], pp. 2–22). Specifically, significant advances have been made to identify the chemical link that specific microbes have with some minerals that appear to precipitate within microbial mats. Seven examples are: (1) *Synechococcus* sp.-precipitating gypsum, calcite, and magnesite [25]; (2) isolated bacteria-precipitating arsenic sulfides [26]; (3) *Virgibacillus marismortui*- and *Marinobacter* sp.-precipitating dolomite [27]; (4) calcium carbonate production due to extracellular polymeric substances (EPS) and low-weight organic carbon molecule degradation [28]; (5) sulfate-reducing bacteria (SRB) promoting calcium carbonate nucleation and growth [29]; (6) sequential formation of Mg-rich carbonates through the decay of organic matter by a fermentative EPS-forming bacterium, *Desemzia incerta* [30]; and (7) cyanobacterially induced silicification due to EPS and pH changes in the presence of magnesium cations (Mg^{2+}) and >70 ppm silica [31]. These studies are limited, as they used specific, isolated biological material, which does not have the properties (quorum-sensing interactions, symbiosis) of the microbial consortium (biocomplexity conundrum). An alternative to that would be to recreate a microbial community by growing each type of organism and mixing all of them, but this is not feasible yet, as many of the micro-organisms have not been isolated [32,33]. Another limitation of these studies is that more minerals are detected within microbial mats in nature than in these specific experiments (usually a few phases). This can be noticed, for instance, when comparing minerals detected in natural microbial mats [15–17] with isolates from the same mats [30], both from a common source. Isolates miss some minerals and therefore seem not to precipitate complete mineral paragenesis found within microbial mats. Experiments with specific bio-organic components have helped with predictions and shortcomings, but they were, by necessity, limited to single-component simplifications of the complex microbial system [34]. Thus, the biocomplexity of the microbial-mat community has not been addressed, nor has the effect of environmental change, which is known to promote dynamic behaviors in microbial-mat communities [15,17], and microbially mediated mineral paragenesis [16,17]. Accordingly, there is a gap in addressing the function of the full microbial community in bio-induced and bio-influenced mineral precipitation.

We studied microbially induced and influenced mineral paragenesis occurring in saline ponds by cultivating and monitoring microbial mats collected from two salt flats.

We are not aware of other studies in which mineral precipitation has been monitored in laboratory microcosms of complete microbial-mat communities.

Overview of Sites

Salar de Pajonales (PAJ) and Salar de Gorbea (GOR) are intravolcanic salt flats that extend along the Andes at 3500 and 4000 m above sea level, respectively (Figure 1). PAJ ($25^{\circ}08'43''$ S, $69^{\circ}49'12''$ W) and GOR ($25^{\circ}24'36''$ S, $68^{\circ}40'31''$ W) areas are 104 km^2 and 30 km^2 , within larger catchments of 2000 and 320 km^2 , respectively. Andesitic and dacitic stratovolcanoes surround the basins [35–38]. PAJ is near Lomas de la Peña and Quebrado volcanoes of the Middle to Upper Miocene age [39], whereas Gorbea is bounded by Lascarria, Plato de Sopa, and Cerro Bayo volcanoes, which are part of the Miocene–Holocene volcanic arc [38].

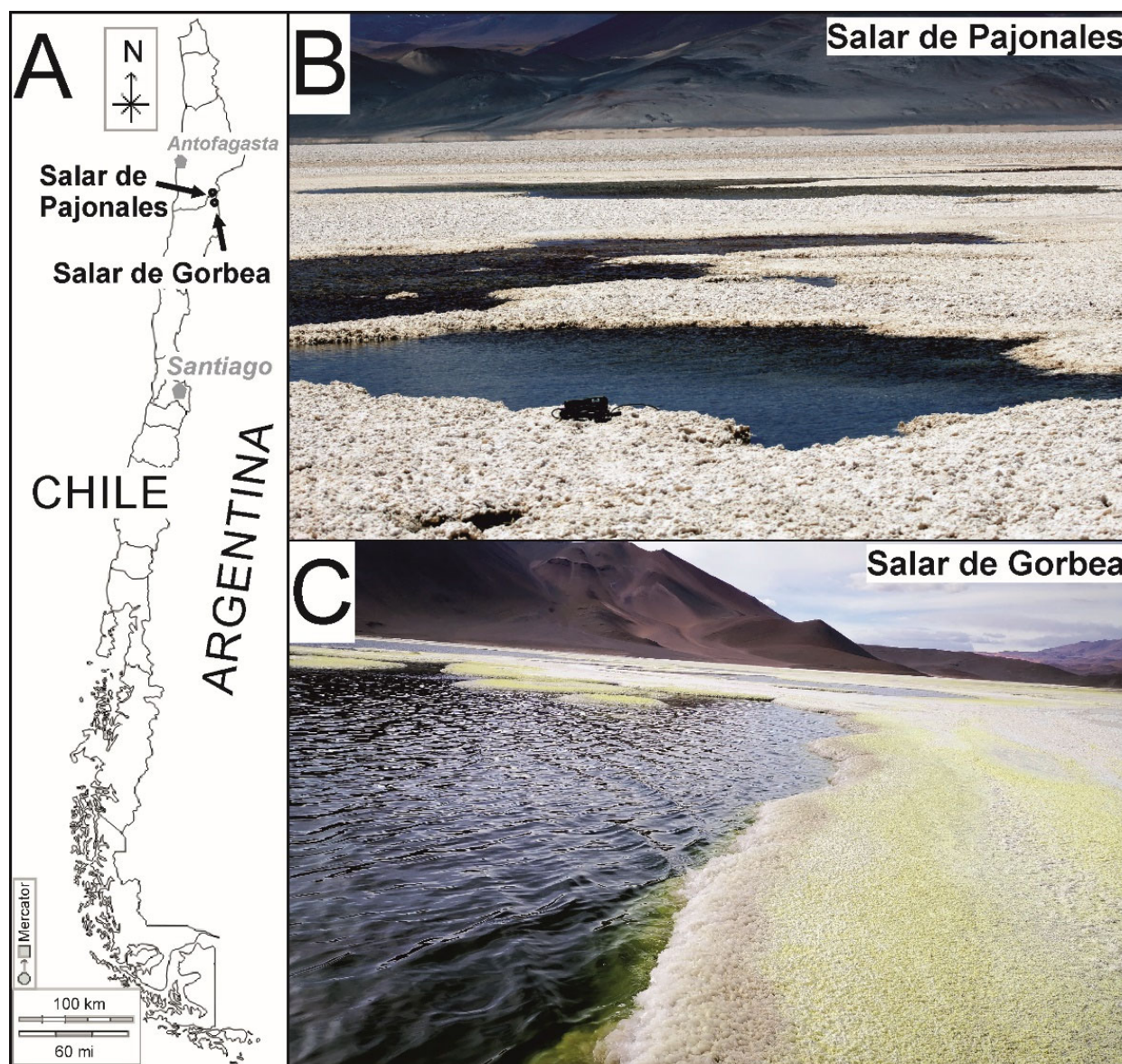


Figure 1. (A) Location of the sampling sites in Chile. Overview images of the salt flat ponds in Salar de Pajonales (B) and Salar de Gorbea (C). Note: white and yellow mineral crusts are comprised mainly by gypsum and halite in (B) [23,37,40] and gypsum mixed with Al-Mg and K-Fe sulphates in (C) [38].

Climate in these areas is extreme, and conditions are characterized by large seasonal and diurnal temperature ranges, strong winds, high evaporation rates, and scarce rainfall or snowfall (300 mm/yr). This region of the Andean Cordillera has no historical record of site-specific weather or climate due to its remoteness, lack of permanent settlements, and poor accessibility [41]. However, observed physiographic conditions and climate data from lower elevations in the Atacama Desert [35,37,38,42–44] to the west of the Cordillera can be used to infer it. Some data are available for the Chilean Altiplano, including evaporation rates (up to 1500 mm/yr) [43] and the world's highest solar radiation flux (ca. 310 W/m², reaching up to 6.6 KWh/m²d) [45]. Despite its dryness, the Altiplano is occasionally subjected to cooling [44,46], which produces flooding and destruction during intense rainfall events ([44,47] and references therein). Extreme climate makes these areas excellent analogs for Early Earth and Mars [4,36].

Both salt flats are hydrologically active evaporitic systems that have experienced notable climatic changes since their origin, and nowadays, they are in transit to a more arid climate, severely affected by anthropogenic climate change and by overconsumption of water resources [37,48]. These changes have left an evaporitic deposit several meters thick and configured a landscape with a multitude of characteristic geomorphological features, e.g., polygon ridges; polygon cracks; hummocks, mounds, tumuli, or domes; quasi-flat areas; dunes and cauliflower-like crusts [38,41,48,49].

These two salt flats comprise typical saline environments with similar geochemistry, but distinct microbial populations [50–53], in scattered water pools that undergo wetting and drying cycles (Figure 1). Brines are enriched in calcium, sulfate, sodium, chloride, and magnesium, with minor amounts of iron and aluminum [35,38,52,53]. The ions of the brines that fill these pools come from a combination of atmospheric aerosols, volcanic emissions, and chemical weathering, and they are concentrated due to evaporation [35,37,38,54,55]. The water received by the basins, comes from precipitation runoff [35] and groundwater [37,38,56]. Waters in both salt flats have wide salinity ranges (1–28%), whereas pH is acidic in GOR (~1–5) and acidic to alkaline in PAJ (~5–9). Many different phases were identified within the sediments near and inside the pools [23,37,38,40,41]. Gypsum (CaSO₄·2H₂O), halite (NaCl), and hexahydrite (MgSO₄·6H₂O) were found in both salt flats. Ulexite (NaCaB₅O₆(OH)₆·5H₂O) and calcite (CaCO₃) were only found in PAJ. Epsomite (MgSO₄·7H₂O), starkeyite (MgSO₄·4H₂O), and carnallite (KMgCl₃·6H₂O), as well as minor to trace amounts of kainite (KMg(SO₄)Cl·3H₂O), tachyhydrite (CaMg₂Cl₆·12H₂O), Mg-aubertite (MgAl(SO₄)₂Cl·14H₂O), and jarosite (KFe³⁺₃(SO₄)₂(OH)₆) were found in GOR. Among the known microbes, the genera *Proteobacteria*, *Bacteroidetes*, and *Cyanobacteria* (mainly species of *Chroococciopsis* and *Dactylococopsis*) dominate the microbial population of sediments and water in PAJ, whereas in GOR, the population is dominated by *Proteobacteria*, *Firmicutes*, and *Actinobacteria* [50–53]. Both salt flats support eukaryotes (diatoms and other algae), sometimes as true endoliths inside fluid inclusions within crystals [57].

2. Methodology

Several biogeochemical techniques were combined to monitor time-controlled samples. Physicochemical measurements, together with microbial mat fabric observations were done. Micro-organisms were observed in optical microscopy, and paragenesis of the minerals was characterized by scanning electron microscopy and X-ray diffraction (Figure 2). Non-evaporitic and evaporitic brine controls were also analyzed using the same techniques to differentiate minerals in association with and without whole microbial communities and the organic substances derived from them, i.e., EPS (extracellular polymeric substances).

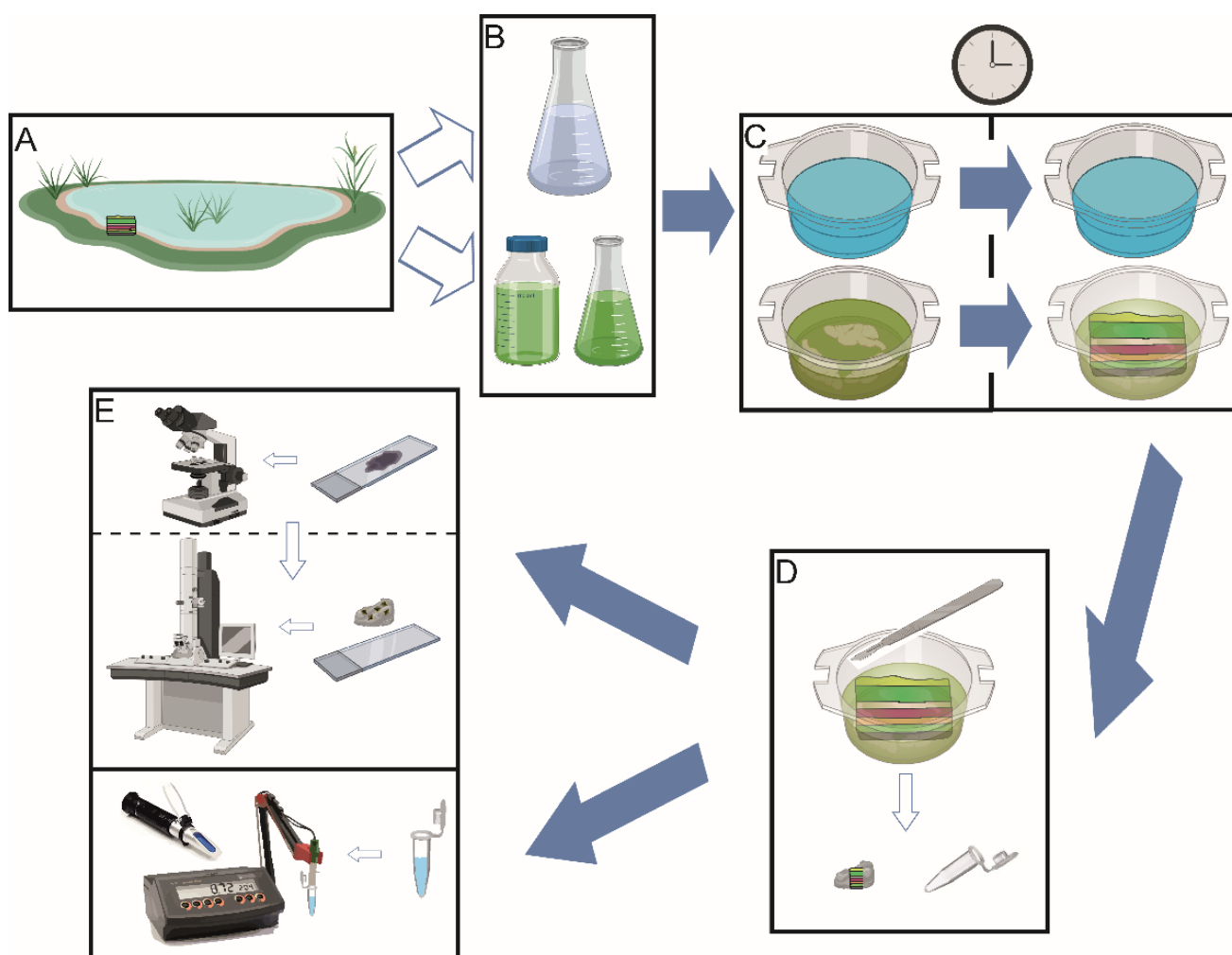


Figure 2. Flow chart of the experimental design. (A) Sampling collection from pond edges (selected areas of the salt flats). (B) Two types of samples collected: water samples (blue flask) and microbial mats (green flask and green bottle). (C) Incubations using microbial mats (green) and controls (blue) evolving through time and growing biomass (green). (D) Subsampling of water from incubations and controls (Eppendorf) and microbial mats/minerals (fragment). (E) Observations of microbial mats/minerals under optical microscopy (**upper**) and electron microscopy (middle), as well as salinity/pH determinations (**lower**).

2.1. Field Work, Sample Collection, and Water Analysis

More than 50 water column samples (1–5 L) and tens of non-lithified microbial mats (100–500 g) were collected at the edges of the ponds and shallow pools in four field campaigns over the course of a week between 2018 and 2020. For this study, 12 water samples were selected for each salt flat, in which, at least, one microbial mat sample was collected (Figure 3). Data collection resulted in 12 microbial mat samples from GOR and 15 sampling sites from PAJ. Microbial mats were unconsolidated, and a few of them were slimy and gelatinous, filled with bubbles. Samples were stored in the dark at 4 °C, and they were processed within 15 days. Water conductivity and pH were measured with a Hanna HI 9829 multiparametric sampler, and salinity was determined using an NaCl refractometer (Atago, Tokyo, Japan).

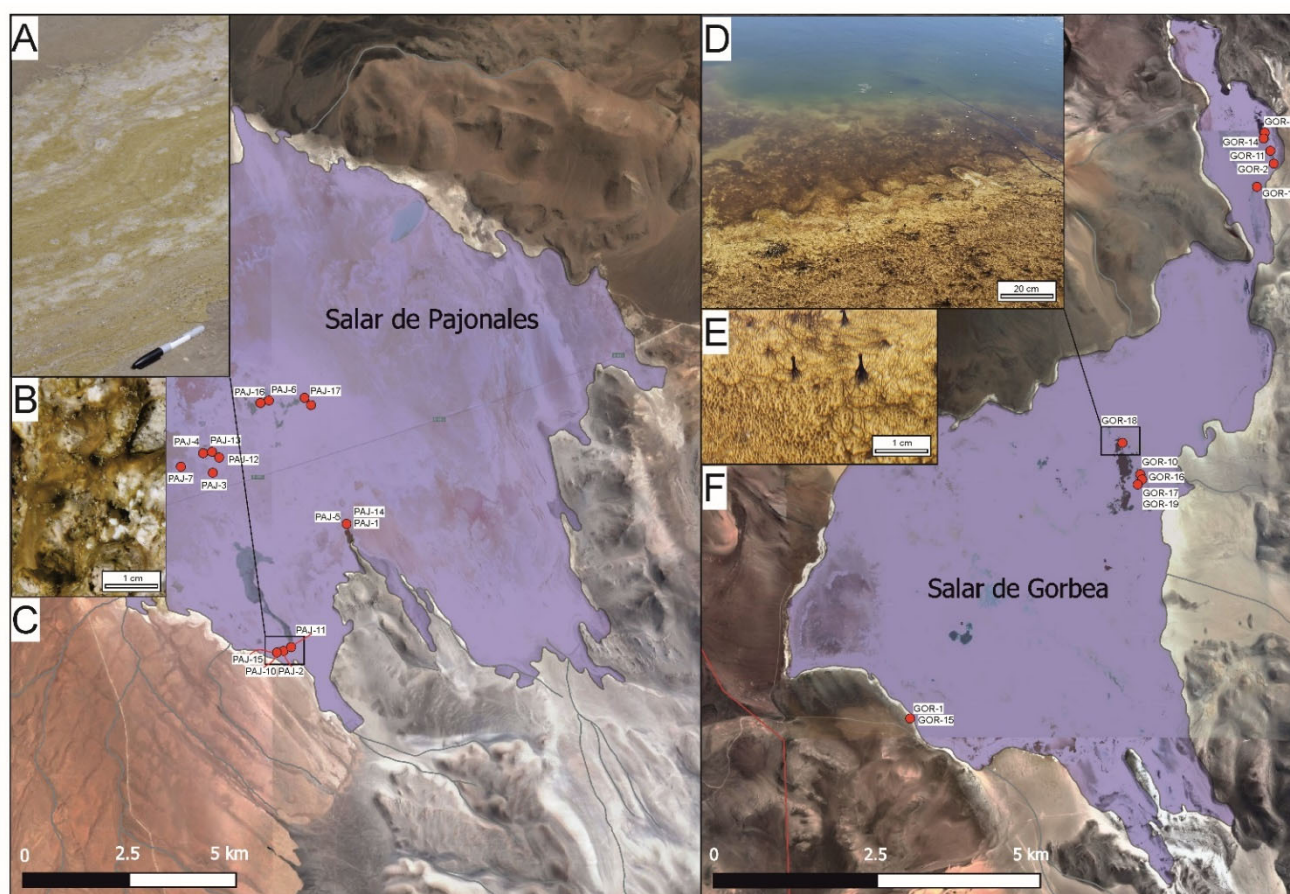


Figure 3. Field photographs showing a representative sample area surrounding the ponds (darker blue zones in the map) of Salar de Pajonales (A), a detailed view of sediments in the sampled area (B), and a view showing the location of sampling points (red dots) in QGIS 3.12.3 (C). Imagery from Google Satellite. The same type of photographs and a map for Salar de Gorbea (D–F). Note the slimy appearance of dark green microbial mats in the surface of the sediments (A,B,D,E). The salar area is overlaid in purple, and grey lines correspond to drainage networks in (C,F). Dark areas inside the purple layer are water bodies, whereas the other parts are mainly sediments.

Water samples were filtered through 0.22 μm pore-size filters (Millipore, Burlington, MA, USA), and 6 of them (PAJ-1, PAJ-7, PAJ-10, PAJ-13, GOR-1, and GOR-2) were analyzed separately for ion compositions (Na^+ , K^+ , Ca^{+2} , Mg^{+2} , Al^{+3} , SiO_2 , Mn^{+2} , and total Fe; Table 1) by an atomic absorption spectrophotometer (Spectra AA 55B-Varian, Varian Inc., Sydney, Australia). B^{+2} and Li^+ were measured by inductively coupled plasma atomic absorption spectroscopy (Perkin-Elmer Optima 2000, Perkin-Elmer, Waltham, MA, USA). HCO_3^- and CO_3^{2-} concentrations were determined through titration by the Mohr volumetric method. Cl^- and SO_4^{2-} were determined by BaCl_2 gravimetric methods. Water compositions were modeled to obtain the saturation indices (SI) for minerals with the Phreeqc 3.7.1-15876 geochemical modeling code [58]. SI is defined by $\text{SI} = \log(\text{IAP}/\text{Ksp})$, where IAP is the ion activity product of the dissolved mineral constituents in a solubility product (Ksp) for a mineral. Thus, $\text{SI} > 0$ implies supersaturation concerning for a mineral, whereas $\text{SI} < 0$ means undersaturation. Main minerals were selected based on previous field studies [23,37,38,40,41]. Due to the high salinity of the lake waters, Pitzer equations were used for calculation [59]. Solution calculations were performed considering the physicochemical values of temperature and pH.

Table 1. Physicochemistry, hydrochemistry, and geochemical modeling of representative brines from Salar de Pajonales and Salar de Gorbea. Pitzer equations were used for saturation indices (SI). Supersaturated values in bold.

Salar		Pajonales				Gorbea	
Sample		PAJ-10	PAJ-1	PAJ-7	PAJ-13	GOR-2	GOR-1
Salinity	% w/v	1.9	4.0	17.3	24.2	1.2	10.6
Temperature	°C	11.1	13.6	14.3	19.8	11	9
pH		7.7	8.0	7.3	6.6	4.6	3.3
Na ⁺	mg/L	3680 ± 368	107,85 ± 1078	51,760 ± 5176	100,220 ± 10,022	2250 ± 225	9511 ± 951
Mg ²⁺	mg/L	223 ± 22	561 ± 56	3090 ± 309	5840 ± 584	16 ± 2	8760 ± 876
Ca ²⁺	mg/L	678 ± 68	2326 ± 233	6895 ± 690	9985 ± 999	370 ± 37	600 ± 60
K ⁺	mg/L	210 ± 21	340 ± 34	2150 ± 215	2670 ± 267	250 ± 25	1224 ± 122
SiO ₂	mg/L	67 ± 7	69.5 ± 7	72.5 ± 7	78.9 ± 7	134.1 ± 13	103.1 ± 10
Cl ⁻	mg/L	7397 ± 740	20,460 ± 2046	104,000 ± 10,400	198,700 ± 19,870	3700 ± 370	37,970 ± 3797
SO ₄ ²⁻	mg/L	470 ± 47	1320 ± 132	2240 ± 224	760 ± 76	1090 ± 109	12,000 ± 1200
HCO ₃ ⁻	mg/L	63.7 ± 6	95 ± 10	49 ± 5	92 ± 10	0	0
Calcite SI	log Q/K	0.3	1.2	1.1	1.9	-	-
Gypsum SI	log Q/K	-0.8	-0.2	0.2	0.4	-0.5	-0.2
Halite SI	log Q/K	-3.3	-2.5	-0.8	0.4	-3.8	-2.2
Opal SI	log Q/K	-0.3	-0.2	0.1	0.8	0.0	0.1
Sepiolite SI	log Q/K	1.1	3.1	3.8	6.2	-12.6	-12.4

2.2. Experimental Setup: Intact Microbial Mat Manipulations

Gelatinous pieces of non-lithified and slimy microbial mats (gels) were picked up from their original field containers. These were first purified by motion, gently shaken, decanted using their corresponding water (sampling site), and transferred to remove precipitates. Purification was verified by bright-field observations (Supplementary Figure S15) with a FV1000 confocal laser-scanning microscope (CLSM; Olympus, Japan). The mats were placed in autoclaved (121 °C) glass containers (8 cm × 8 cm × 5 cm) and covered with plastic petri dishes.

Microbial gels were positioned either directly on the bottom of the container or on a thin layer (50 g) of sterile gypsum as a substrate. Some of the mat samples were split into two (or more) incubations under different conditions, and they were labeled with ‘*.1’ and ‘*.2’, resulting in 21 and 13 incubations from PAJ and GOR, respectively (PAJ-1 to PAJ-17 and GOR-1 to GOR-17 incubations in Supplementary Table S1). Gypsum substrates were prepared by selecting well-developed prismatic crystals (c-axis size >20 cm). These crystals were brushed clean to remove smaller crystals and twins, and they were crushed using a mortar and pestle. In situ observations suggested the use of fine and coarse gypsum substrates for PAJ incubations, whereas only coarse gypsum substrate was needed for GOR incubations. Therefore, crushed crystals were subdivided using a mesh to a fine substrate (<1 mm) and a coarse substrate (>1mm). Substrates were characterized by electron microscopy to enable morphological distinction from new mineral precipitates (CG and FG samples in Supplementary Table S1).

The containers were filled with approximately 200 mL of 0.22 µm filtered lake water to maintain the ionic composition of the study site and incubated in a culture chamber with light and air circulation. The chamber was placed in a room subjected to the slight environmental changes of Antofagasta city. Therefore, the temperature and relative humidity inside the chamber fluctuated from 17 °C and 54% in winter to 25 °C and 59% in summer, respectively. Day and night were simulated by alternating twelve-hour periods of illumination and darkness with 12 LED lamps (6000K, 18 W, Unilux, Shanghai, China), generating light intensities >200 µE·m⁻²·s⁻¹.

Water levels were drawn with permanent marker in every container, and samples were episodically replenished with deionized water to keep levels constant and avoid precipitation due to evaporation. To evaluate the response of the microcosms through time, pH and salinity were measured by extracting brine seven times for 18 months. To minimize the impact of brine extraction, only ~1 mL from each container was subtracted without replenishing each time, so >95% of the original brine was kept after two years of nursing.

Control containers were filled with filtered brine only and episodically monitored. To reduce the number of samples, PAJ-10 to PAJ-17 control brines were skipped, resulting in 4 and 12 controls from PAJ and GOR, respectively (CPAJ-1 to CPAJ-7 and CGOR-1 to CGOR-19 in Supplementary Table S1). To simulate evaporation and verify mineralogy, one of the controls (CGOR-1) was allowed to evaporate. Distilled water was not replenished in order to simulate the slow evaporation process expected during periods of drying, so 4 and 11 non-evaporated controls were kept from PAJ and GOR, respectively. These controls were not subjected to brine extraction for salinity and pH monitoring in order not to affect mineral precipitation during evaporation.

Microbial mat samples and controls were episodically photographed with Huawei-Leica smartphone cameras (Shenzhen, China) and observed to detect textural changes and mineral precipitation. Small subsamples (2 mm²) of the microbial mats were also episodically subtracted from the upper part (1 cm of depth; free of substrate) to document changes and confirm observations. Subsampling was performed using a sterilized scalpel to excise the mats, minimizing their destruction (Figure 3). Additionally, non-evaporated controls were episodically subsampled for verification of their precipitates by optical microscopy.

2.3. Optical and Electron Microscopy

Cell morphotype, autofluorescent pigment, and brief mineral precipitation analyses were carried out by placing subsamples in microscope slides (24 mm × 50 mm × 0.15 mm, Pearl 7101, Leica, Wetzlar, Germany) immersed in type-F oil. These subsamples were observed in bright-field and fluorescence modes with a CLSM FV1000 instrument (Olympus, Japan) equipped with a 100x Plan-Apochromat IX-81 oil-immersion objective lens (Olympus, Japan) and an HBO 100W Hg lamp burner (Olympus, Japan) to emit wavelengths from 400 nm to 800 nm. The red autofluorescence of photosynthetic pigments was used as a photosynthetic activity marker of oxygenic photosynthesis in the microbial mats. Cell and diatom morphotypes were described and classified based on previous studies and manuals [20,60,61], ([24] pp. 511–526). A field emission scanning electron microscope coupled with energy-dispersive X-ray spectroscopy (FE-SEM-EDX, SU5000, Hitachi, Tokyo, Japan) was used to determine the morphology of the precipitates on subsamples previously passed through an instant-immobilization stage before cell death using a fixation–dehydration process. This process consisted of fixation with 4% paraformaldehyde using 0.22 µm filtered saline water at room temperature overnight and then dehydration stages with ethanol solutions at 20%, 40%, 60%, 80%, 90%, 95%, 98% and 100% at one-hour intervals in a laminar flow chamber (ESCO model AC2 -6E8 class II BSC, Singapore). The subsamples were gold-coated with a Desk II model sputter coater Denton Vacuum LLC, (Moorestown, NJ, USA).

2.4. X-ray Diffraction

Subsamples were dehydrated with absorbent paper, and minerals were semi-quantified by X-ray diffraction using a Bruker D8 Advance diffractometer under monochromatic Cu-K α radiation ($\lambda = 1.5406 \text{ \AA}$) operating at 40 kV and 30 mA, a step size of 0.02° 2 θ , and time per step of 2 s. Diffractograms were interpreted using EVA Bruker and ICCD software with the PDF4+ 2021 database. Organic matter and amorphous phases generated noise, making interpretation difficult, so the diffractogram was smoothed, and the baseline was corrected to improve semi-quantification.

2.5. Data Processing

Categorical variables (substrates: no substrate, fine gypsum, and coarse gypsum; salt flats: PAJ and GOR; turbidity; EPS color and consistency: loose and dense white/green/orange/brown gels; bubble occurrence; microbial structure evolution: e.g., colorful layers of different thicknesses, no structure, smooth gels, pinnacles, and domical structures) and numerical values (pH, salinity) were recorded at each sample interval. Primer6 software (New Zealand) was used to compare the variables according to the resemblance of Euclidean distances of normalized parameters and plotted using principal coordinates analysis (PCO). The PCO plot had 65.7% and 33.6% variability for the first and second principal coordinates (PCO1 and PCO2), respectively.

3. Results

Laboratory experiments involving growing microbial mats in microcosms with and without gypsum substrates yielded the same suite of major minerals observed in the natural system of salt flat ponds [23,37,38,40,41]. Microbial and physicochemical checkups over time were used to monitor biogeochemical changes. The minerals precipitated in the microbial mats and the morphologies described in comparison with controls without microbes differentiated biotic and abiotic participation. Additionally, geochemical modeling, which helps to predict mineralogy, was compared to the minerals obtained within the experiments (supersaturated salts should precipitate, whereas undersaturated salts should dissolve). Summarized results are presented for simplicity, connecting sample observations to improve readability. Additionally, details of each individual sample can be found in Supplementary Table S1 and Supplementary Figures S1–S15. The figures cover a representative view of main observations summarized in Supplementary Table S1.

3.1. Field Measurements and Geochemical Modeling

Measurements of the physicochemistry performed in the field showed that the salinity of the water ranged from 1.9% *w/v* to 24.2% *w/v* and from 1.2% *w/v* to 10.6% *w/v*, whereas pH ranged from 6.6 to 8 and from 3.3 to 4.6 for PAJ and GOR, respectively (Table 1). These values were obtained between 11.1 °C and 19.8 °C in PAJ brines and between 9 °C and 11 °C in GOR brines.

Geochemical modeling carried out using PHREEQC (Table 1) indicated supersaturated and undersaturated phases that can be theoretically expected to precipitate or dissolve, accordingly. The water of PAJ, with positive saturation indices, was always supersaturated with respect to the calcite ($SI > 0.3$). These fluids were in equilibrium or slightly undersaturated in gypsum (avg. saturation of -0.1) for PAJ and slightly undersaturated for GOR (avg. saturation of -0.4). In most cases, the brines were undersaturated for halite in both PAJ and GOR (avg. saturation of -1.5 and -3 , respectively). On the contrary, the saturation indices for opal ($SiO_2 \cdot nH_2O$) were in equilibrium or slightly positive for PAJ and GOR (avg. saturation of 0.2 and 0.1, respectively) and positive for sepiolite ($Mg_4(Si_6O_{15})(OH)_2 \cdot 6H_2O$) in PAJ (avg. saturation of 3.5). Brines were highly undersaturated in sepiolite for GOR brines (avg. saturation of -12.5).

3.2. Physicochemical Monitoring of Laboratory Incubations

Physicochemistry measurements were used to monitor the water column in the microcosm experiments (Figure 4 and Supplementary Figure S1). Non-evaporitic controls provided a baseline to compare the experiments. PAJ pH increased in the first 30 days and then decreased for between 60 and 80–120 days (Figure 4A,B; Supplementary Figure S1, vertical red lines), and salinity increased or decreased for between 10 and 60 days, and then, reversed direction for some but not all experiments until the solutions stabilized after 80–120 days. Similarly, it appears that GOR solutions did not stabilize for up to 90–110 days. Therefore, a ‘stabilization stage’ of, on average, 100 days was needed after most samples and controls were stabilized (Figure 4C,D; Supplementary Figure S1, vertical red lines). However, these mats showed a minimum ‘stabilization stage’ of approximately

30 days in some of the incubations, which lasted up to 60–120 days in others. The slight fluctuations observed after 100 days in controls without evaporation and mat containers are attributed to seasonal variations in humidity and temperature of the microcosms (Figure 4; Supplementary Figures S1–S13).

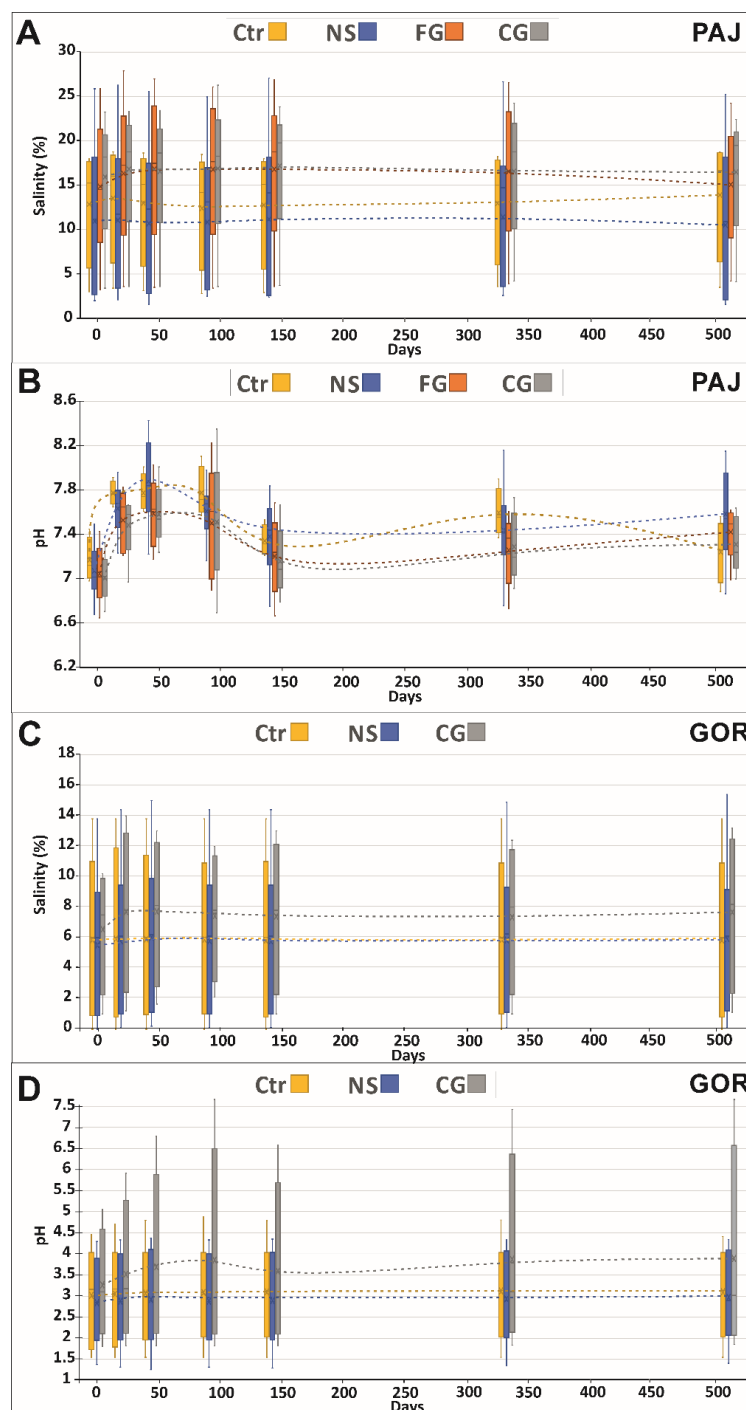


Figure 4. Physicochemistry of Salar de Pajonales (PAJ) (A,B) and Salar de Gorbea (GOR) incubations (C,D). Salinity (A,C) and pH (B,D) of controls (Ctr) and microbial mat samples with and without substrates (NS) over >500 days. The substrates used were fine gypsum (FG) and coarse gypsum (CG). Dashed red lines indicate delimitations of incubation stabilization and stabilized brines after the red lines. Note that different pH and salinity scales were used for PAJ and GOR incubations to maximize the visualization of stabilization fluctuations.

PAJ controls covered a range from 6.8 pH to 7.4 and 4% *w/v* salinity to 18% *w/v*, with small fluctuations of 1 pH and 2 salinity units over the first 100 days (Figure 4A,B; Supplementary Figures S1–S9). In contrast, larger fluctuations were observed in microbial mat samples than in controls (Figure 4A,B; Supplementary Figure S3). Specifically, non-substrate samples, covering a range from 6.2 pH to 8.2 and 4% *w/v* salinity to 25% *w/v*, fluctuated by up to 1.5 pH units and 4 salinity units, respectively (Figure 4A,B). Samples with fine and coarse gypsum substrates fluctuated similarly, although they reached a slightly higher salinity (26% *w/v*) and pH (from 6.7 to 8.5). From 100 to 330 days (Supplementary Figure S1, vertical yellow lines), controls and microbial mat samples kept their salinity, and salinity, in the controls, increased slightly from 330 to the end of the experiment, whereas it decreased in mat samples (Figure 4A). In the period from 100 to 330 days, pH increased slightly for both controls and microbial mat samples, whereas it decreased from 330 to values below the starting value, at the end of the experimental period (Figure 4B).

GOR controls covered a range from 1.8 pH to 4.5 and 1% *w/v* salinity to 14% *w/v*, with very small fluctuations of 0.5 pH and 2 salinity units over the first 100 days (Figure 4C,D; Supplementary Figures S1,S10–S13). Larger salinity and pH fluctuations were observed in GOR microbial mat samples than in controls (Figure 4D; Supplementary Figures S10–S12). Specifically, non-substrate samples, covering a range from 1.3 pH to 4.2 and 1% *w/v* salinity to 15% *w/v* fluctuated by up to 2 pH and 2.5 salinity units, respectively. Samples with coarse gypsum substrate fluctuated likewise, although they showed higher pH (from 1.5 to 5) and salinities from 1.5% *w/v* to 10% *w/v*. A sample with a coarse gypsum substrate (GOR-2) was an exception, in which pH values increased by two units (Supplementary Figure S13).

At the beginning of the experiment, no remarkable differences for the averaged pH or salinity were observed in the incubations between different substrates (note close values plotted as points $\langle x \rangle$ between incubation groups in Figure 4 at 0 days). Within 14–43 days, the incubations with no substrate and the controls reached a pH of 4.7 and a salinity of 14.4% *w/v* in those from GOR (Figure 4C,D). Higher values were reached from PAJ, with pH values of up to 8.0 and a salinity of 26% *w/v* (Figure 4A,B). In the whole period monitored, pH and salinity increased by up to 7.5 and 15.4% *w/v*, respectively, in samples from GOR (Figure 4C,D) and 8.0 to 25% *w/v*, respectively, in samples from PAJ (Figure 4A,B).

The principal coordinates analysis (PCO) plot shows three sample groups based on their substrates vs. salinity and pH at the beginning of the experiments (Figure 5): one corresponding to PAJ samples, one corresponding to GOR, and a third group with samples from both salt flats. The growth differences between the microbial mats' incubations were attributed to salinity and, secondarily, to the different substrates used, whereas pH was not correlated.

3.3. Microbial Mat Dynamics

The spatial and temporal development of the communities was monitored episodically for a representative example of each set of experimental conditions. The microbial mats were monitored for mat fabric and the largest micro-organisms by microscopy over the course of the experiments (Figure 6 and Supplementary Table S1).

The higher salinity and pH of the incubations were related to more diverse and colorful morphologies (Figure 6 and Supplementary Table S1), as well as denser, thicker, and homogeneously stratified layers of gels, i.e., gelatinous EPS (e.g., PAJ-7-1 to PAJ-7.3 in Supplementary Figures S3 and S14). This was observed earlier in the experimental period when comparing PAJ and GOR incubations (200 vs. 300 days, respectively). Besides that, PAJ-4.1 and PAJ-5.2 mats which were incubated with highly concentrated brines (18.4% *w/v* and 26% *w/v* at the beginning of the experiment, respectively) did not grow (Supplementary Table S1; Supplementary Figure S6). Conversely, some mats from PAJ grew thicker than those from GOR in shorter times (e.g., PAJ-17 in Figure 6 and Supplementary Table S1). Generally, wide salinity and pH ranges within incubations of the same salt flat

resulted in more differences in the mat growth than in the comparison between PAJ and GOR incubations (Supplementary Figure S1 and Supplementary Table S1).

Most of the samples were turbid and formed a loose gel in the first days of the experiment (e.g., PAJ-10 incubation in Figure 6A). This was reflected by a bloom of planktonic organisms, mainly diatoms (e.g., PAJ-16 incubation in Figure 6B). Two of the samples (PAJ-3 and PAJ-17) were different, and they showed mainly cyanobacteria that were morphologically compatible with *Dactylococcopsis* sp. (Figure 6C). Some of the samples showed visible floating gels that contained numerous diatoms (e.g., PAJ-14 incubation in Figure 6D). The pH ranged from 6.26 to 7.90, and the salinity ranged from 4 to 20% *w/v* when the gels were first observed (Supplementary Table S1 and Supplementary Figures S5 and S7).

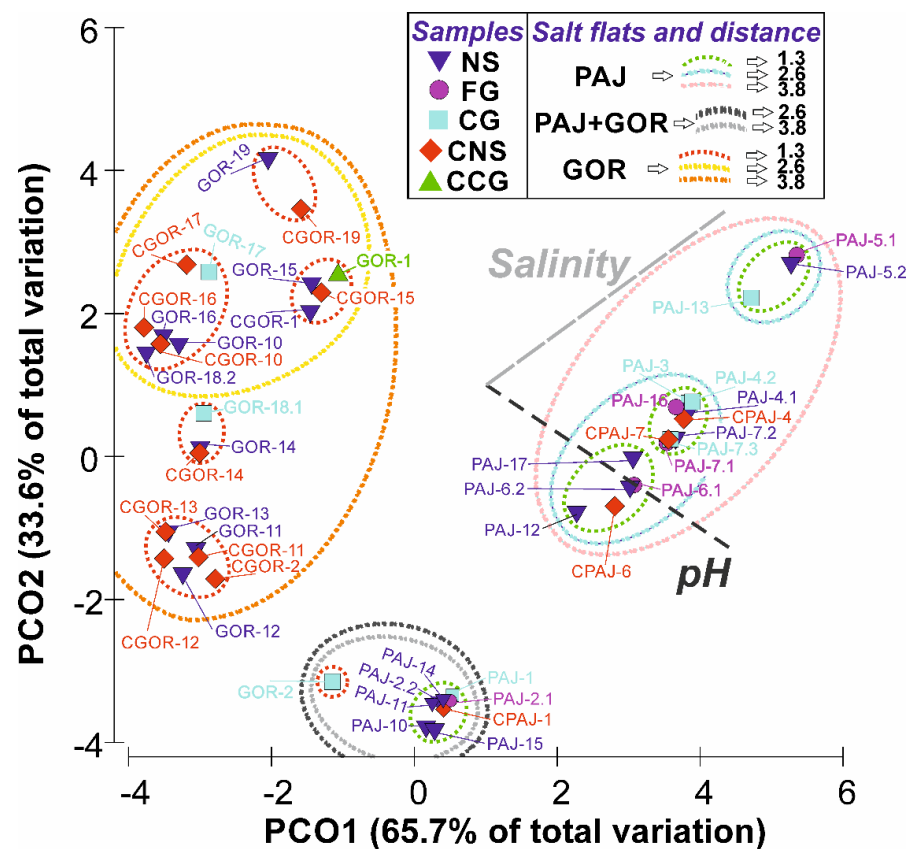


Figure 5. Principal coordinates analysis (PCO) the Euclidian distance matrix of normalized data (pH and salinity from the beginning of the experiment) between samples: no substrate (NS), fine gypsum (FG), coarse gypsum (CG); and controls: control with no substrate (CNS), control with coarse gypsum (CCG) from Salar de Pajonales (PAJ) and Salar de Gorbea (GOR) during the incubation time. The graph shows the meaningful relationship (distance) between samples as close (1.3), intermediate (2.6), and distant (3.8). Samples with high salinity and pH values loaded positively on the PCO1, whereas low-salinity and low-pH values loaded negatively on PCO1.

After 30 days, EPS gels were reduced in the water column of many of the samples (except PAJ-11, PAJ-16, PAJ-17, GOR-12, GOR-13, GOR-16, GOR-18.1, GOR-18.2, and GOR-19, Supplementary Table S1), and the upper part of the containers cleared (e.g., PAJ-16 incubation in Figure 6E). The largest micro-organisms, mainly diatoms, were significantly smaller in this upper part in comparison with micro-organisms observed at the beginning of the experiments, and the benthic communities were more colorful (not shown). These changes resulted in semi-cohesive and cohesive stratified microbial mats with plain to gently convex surfaces (like those observed in the field, as in Figure 3D) of versicolored layers (i.e., bright green, orange, brown, and deep black; summarized in Supplementary Table S1). PAJ-15 and PAJ-16 incubations had blooms of yellowish color. Many other

incubations showed whitish color instead (e.g., GOR-2, PAJ-1, etc.; Supplementary Table S1). Both yellow and white growths had a gelatinous consistency (e.g., PAJ-16 incubation in Figure 6E; Supplementary Table S1). Among the organisms that stood out in these samples, diatoms of various genera, such as *Amphora*, *Navicula*, *Nitzschia*, and *Cocconeis*, among others, were observed (Figure 6B,D,F–H).

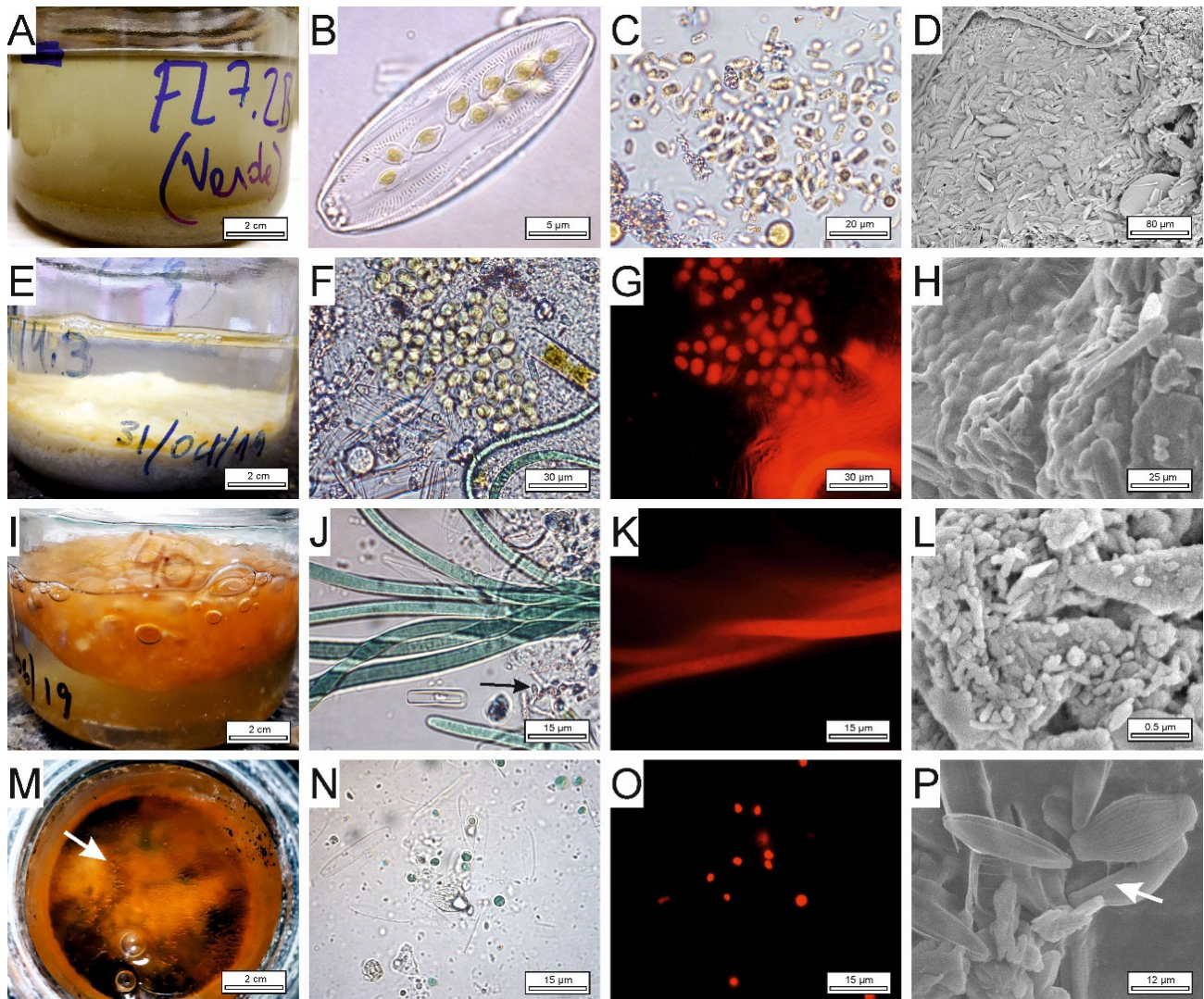


Figure 6. Set of representative macromorphological and microscopic checkups for Salar de Pajonales (PAJ) and Salar de Gorbea (GOR) microbial mat containers from the beginning of the experiment to >500 days. (A) Side view of PAJ-11 container with a cloudy water column 7 days after starting the experiment. Bright-light microphotographs showing that clouds were due to 4 μm diatoms in cell division, such as *Amphora* genus morphotypes, from the PAJ-16 incubation (B) and compatible with *Dactylococcopsis* genus colonies from the PAJ-17 incubation (C). (D) Field emission scanning electron microscope (FE-SEM) photomicrograph of *Bacillariophyceae* distinctly shaped diatoms (mat crowded predominantly by *Amphora*, *Navicula*, and *Cocconeis* genera) without mineral precipitates in the PAJ-14 incubation. (E) Side view of whitish-to-yellowish PAJ-16 mat incubated with fine gypsum substrate after 30 days. The mat was firmly attached to the substrate, retaining gas bubbles under the gels below a clear water column. (F) Spherical, unicellular cyanobacterial cells (10–15 μm) compatible

with *Chroococidiopsis* genus shown in a bright-light microphotograph in the PAJ-12 incubation. Two filaments compatible with *Oscillatoria* genus and algae individuals are also shown. (G) The same view as (F) under an HBO 100W Hg lamp burner in which photosynthetic pigments were excited, showing autofluorescence of the cells. (H) FE-SEM microphotograph displaying a similar view as (F,G) of coccoid cells agglutinated in extracellular polymeric substances (EPS) in the PAJ-12 incubation. (I) Side view of orange detached/floating mat of PAJ-17, packed with gas bubbles, incubated without substrate after 60 days. (J) The orange gel contained many micro-organisms. Among the observable micro-organisms, long cyanobacterial filaments, diatoms, and sulfur-oxidizing bacteria (black arrow) with visible intracellular sulfur globules compatible with *Oscillatoria*, *Navicula*, and *Chromatium* genera, respectively, stand out, as seen by bright light. (K) The same view as in (J) under an HBO 100W Hg lamp burner. (L) FE-SEM microphotograph of nanometric oval-shaped and bacillar micro-organisms from the GOR-2 incubation. (M) Overhead view of the layered PAJ-11 mat, which developed pinnacle structures (white arrow) after 300 days of incubation. Bright-light (N) and fluorescence microphotographs (O) of unknown 2–5 μm spherical, fluorescent cells and diatom cells compatible with the *Nitzschia* genus in the GOR-16 incubation. (P) FE-SEM microphotograph of 20 μm diatoms resembling the *Amphora* genus embedded within a sticky EPS (white arrow) in the PAJ-12 incubation.

In addition to diatoms, microbes with morphologies consistent with bacteria were observed after 60 days (Figure 6F–H). PAJ-17 sample produced a very consistent orange mat with abundant gas bubbles (Figure 6I) in the lower part of the container. Under a microscope, abundant filamentous cyanobacteria (Figure 6J,K) and diatoms were observed, alongside sulfur-oxidizing bacteria compatible with *Chromatium* sp. (Figure 6J), and other colonies of much smaller organisms (like those observed in the GOR-2 incubation, as in Figure 6L). Some samples (e.g., PAJ-11 and PAJ-12 incubations) exhibited colors from bright green to dark green on which coccoidal and filamentous cyanobacteria dominated (Figure 6F,G,J,K). Both the orange and greenish microbial mats exhibited abundant bubbles around (Figure 6M) and within the gels (Figure 6I).

Most of the samples showed microbial mat growth of several millimeters in thickness after 300 days (not shown). GOR-16, among other samples, showed numerous photosynthetic cocci (Figure 6N,O) and a few filamentous cells (not shown), which were identified by their intense autofluorescent pigments at 680 nm in CLSM and determined to be phycobiliproteins and chlorophyll pigment peaks.

Finally, after 1 year, several of the mats had ca. 1 cm of new growth of EPS gels that could not be dispersed in water or detached with forceps but could be cut with a scalpel (not shown). These gels comprised binding filaments between organisms of various types (as in the PAJ-12 incubation; Figure 6P). Some microbial mats developed small vertical structures (<1 cm), often called pinnacle structures. Likewise, the surfaces of some mats across all experiments changed from a greenish to orange color (e.g., the PAJ-11 incubation in Figure 6M). In contrast, the other colorations remained practically unchanged or darkened slightly (checkup colors through time in Supplementary Table S1). Light and electron microscopy observations revealed that the dominant larger organisms in the communities changed little (not shown). Abundant gases produced by more developed mats detached from the benthic zone, becoming floating mats (e.g., PAJ-12 incubation in Figure 6I). This occurred more frequently in experiments without substrates (e.g., PAJ-12 incubation). No floating mats were observed in samples with substrates reflecting better microbial attachment and enhanced growth, resulting in thicker mats (not shown). There were no noteworthy changes over 500 days.

3.4. Textural and Mineralogical Composition of Precipitates

The potential of the mats to induce mineral precipitation was evaluated through periodic checks (subsamples) by XRD and SEM.

The main phases precipitated in the experiments were gypsum and halite in PAJ and GOR incubations (Figure 7). In contrast, minor calcite was only found in PAJ incubations

(Figure 7A). Sylvite (KCl) and polyhalite ($K_2Ca_2Mg(SO_4)_4 \cdot 2H_2O$) were only detected in PAJ incubations through XRD (Figure 7B). High halite content in diffractogram images and the detection of sylvite and polyhalite that were not observed in fixed SEM samples evidence that these phases precipitated from residual brine that were contained in microbial mats before the analysis. In addition, some proto-phases of phyllosilicates and amorphous phases were detected through XRD and SEM (Figure 7B).

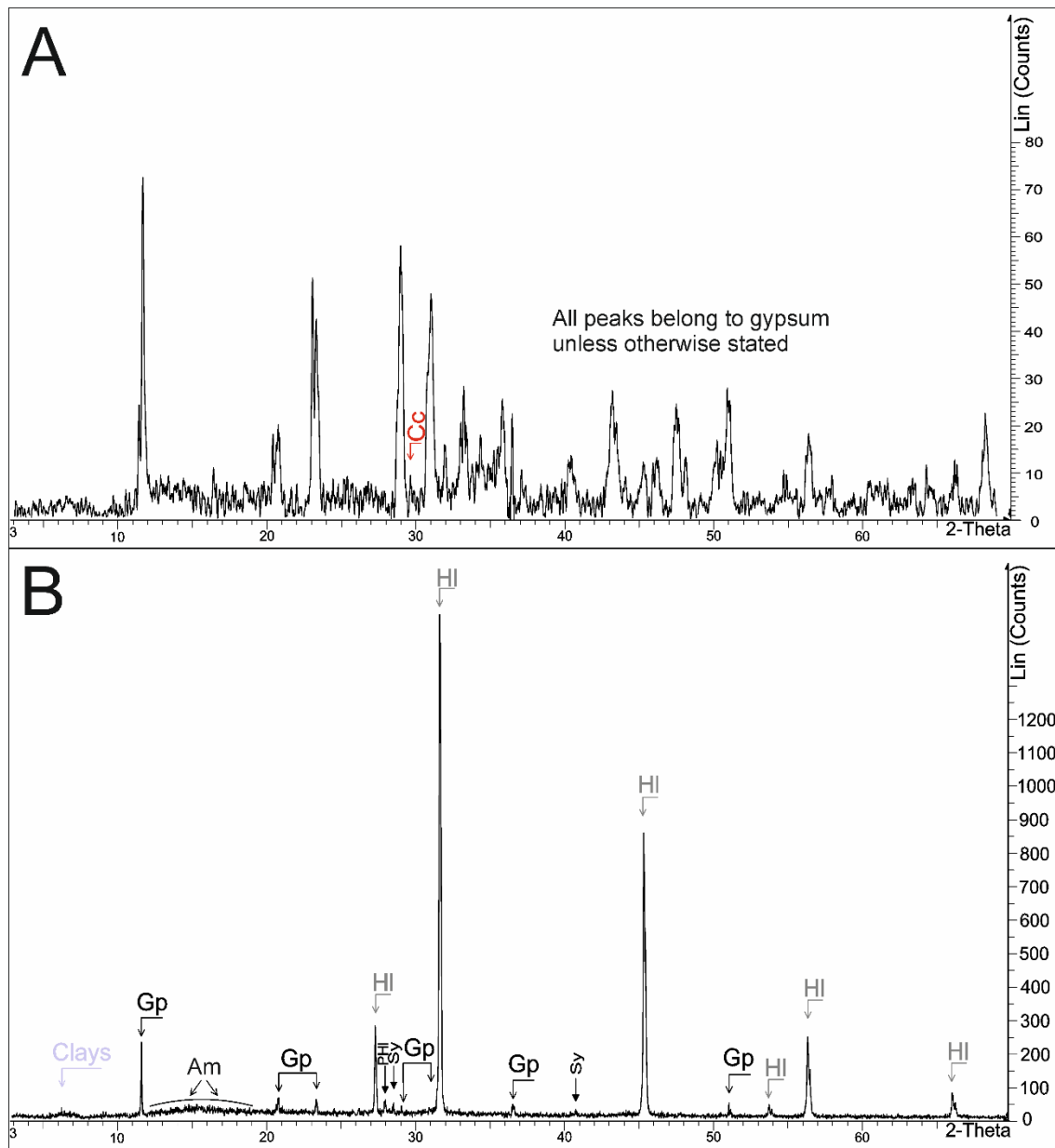


Figure 7. Representative X-ray diffractions of microbial mat samples. (A) Semi-quantification of crystalline phases showed 95% gypsum and 5% calcite (Cc) in a Salar de Pajonales microbial mat (PAJ-10). (B) A second microbial mat from Salar de Gorbea (GOR-16) showed 49% halite (HI), 25% gypsum (Gp), 13% polyhalite (PHI), 11% clay minerals, and 2% sylvite (Sy). Am = amorphous phases (not semi-quantified). Reflection peaks surpass 1200 counts in the GOR mat in contrast with PAJ mat, which shows a lower crystallinity. Note that sylvite, polyhalite, and part of the halite present may be a consequence of the sample preparation. These minerals may have precipitated during the dehydration of interstitial brine contained in the sample.

At the beginning of the experiments, microscopic observations showed that incubations had small amounts of organic matter (micro-organisms plus EPS) and gypsum particles derived from the substrates (Figure 8). No mineral precipitates were observed in the mats, and controls did not show precipitates from their brines either (Supplementary Table S1).

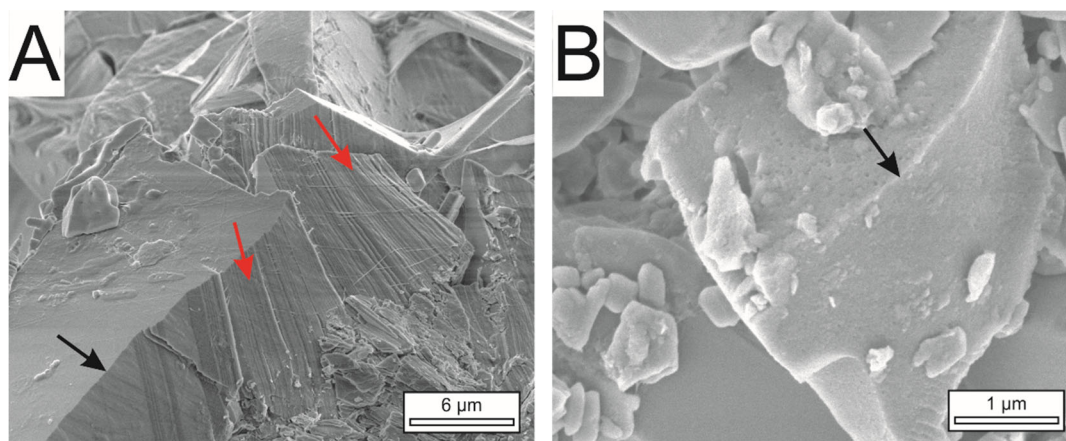


Figure 8. FE-SEM images of (A) coarse-grained and (B) fine-grained substrates. Note the exfoliation planes in the parallel lines of gypsum grains in (A) (red arrows) and imperfect fractures in (A,B) (black arrows).

After 30 days, a few small (<20 μm) hemibipyramidal crystals of gypsum lying over a granulated EPS were observed in the samples (e.g., GOR-2 incubation in Figure 9A; Supplementary Table S1). Over time, crystals became larger and more numerous.

Crystals of gypsum formed in the experiments exhibited four habits: two types of prismatic crystals, lenticular crystals, and acicular crystals. Sixty days after the beginning of the experiment, two sets of prismatic gypsum crystals were observed embedded within the EPS of the samples (e.g., PAJ-11 and PAJ-17 incubations in Figure 9B,C). These crystals grew inside the EPS (Figure 9C) near and below the well-preserved elongated diatom frustules (Figure 9B). The physical properties of the two types of crystals differed. The first type of crystal (Figure 9B) was larger (up to 15 μm) and had a heterogeneous size distribution with a truncated c-axis and occasional single- or double-penetration twins. The second type of crystal (Figure 9C) was smaller (<6 μm) and homogeneous in size, with an elongated c-axis and frequent, parallel twinning overgrowths. A third type of gypsum was observed as dispersed lenticular crystals, >50 μm in size, embedded within soft white-beige EPS (e.g., PAJ-12 incubation in Figure 9D). PAJ-11 and PAJ-12 incubations showed many well-preserved diatom frustules (Figure 9D,E), and PAJ-11 showed some cyanobacterial filaments around gypsum crystals (Figure 9D). Lastly, some elongated, nearly acicular gypsum crystals were observed (e.g., GOR-16 incubations in Figure 9F). These crystals were parallelly twinned and resembled a trichome (stacked cell arrangement within a cyanobacterial sheath).

Halite was present in three forms. The first morphology was halite cements embedding gypsum crystals in some samples (e.g., PAJ-12 incubation in Figure 9D). Secondly, halite crystals were aggregated in small nodules (<6 μm ; e.g., PAJ-17 incubation in Figure 9G) that gradually transformed to larger cubes (20 μm ; e.g., PAJ-17 incubation in Figure 9H). And, lastly, halite also precipitated as aggregates of small, suboctahedral to anhedral crystals (<1 μm ; e.g., GOR-16 incubation in Figure 9I).

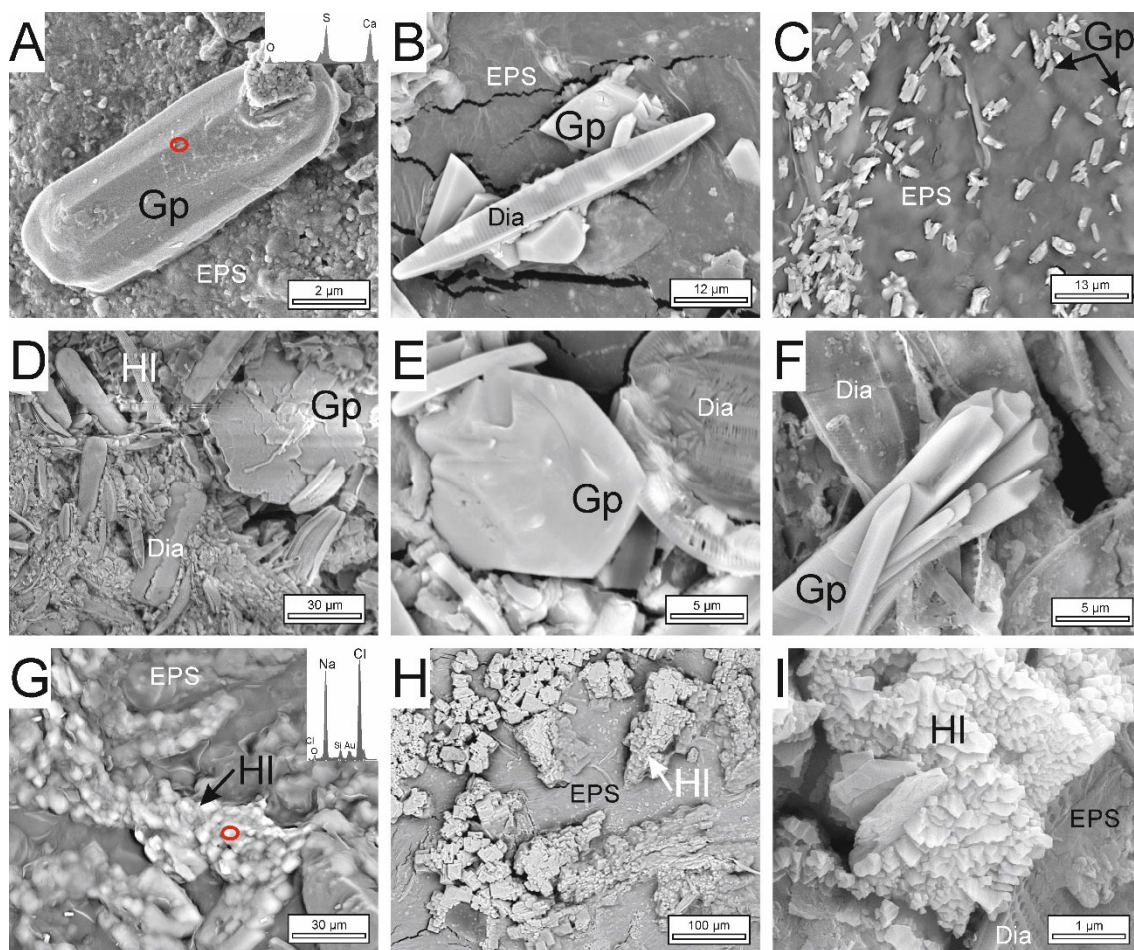


Figure 9. FE-SEM microphotographs of minerals seen in the incubations up to 60 days from the start of the experiment. (A) Hemibipyramidal gypsum (Gp) crystal that precipitated within the first month over granular extracellular polymeric substances (EPS) in a Salar de Gorbea incubation (GOR-2). This granulated morphology was attributed to the numerous coccoid and bacillar cells agglutinated inside the EPS. Energy-dispersive x-ray spectra (EDX) of the red circle point of analyses are displayed as an insert in the upper right corner. (B) Prismatic gypsum crystals with sharp faces protruding from the extracellular matrix (EPS) beside a *Navicula* sp. frustule (Dia) from a Salar de Pajonales incubation (PAJ-11). (C) Prismatic gypsum crystals over EPS from the PAJ-17 incubation. Lenticular gypsum crystals surrounded by large and small diatoms (Dia) of *Amphora* (D,E) in PAJ-12 and *Entomoneis* (E) in PAJ-11 incubations, and small diatoms compatible with *Cocconeis* genus (E), all of which were embedded within EPS. (F) Elongated gypsum crystals diverging from a common nucleating point over a frustule layer (Dia) in a GOR-16 incubation. Note the circular shape of the crystal group resembling filaments. Groups of halite (HI) nodules (G) and euhedral halite cubes (H) embedded within EPS in a PAJ-17 incubation. Note the EDX spectra in (G). (I) Sawtooth-shaped octahedral halite crystals grown from an EPS matrix in a GOR-16 incubation.

After 60 days, globular to subhedral calcite crystals (<50 μm) were observed (Figure 10A,B). They were covered by EPS and partially broken diatom frustules (e.g., PAJ-10 incubation in Figure 10A). These crystals displayed an enormous number of pores <1 μm . These pores resembled cocci and bacilli round shapes, as if they were bacterial external molds, some of which were covered or filled with EPS. Zooming in on a part of a sample where many diatom frustules displayed signs of degradation, rounded grains of calcitic composition were observed (e.g., PAJ-15 incubation in Figure 10B). These calcite grains are compatible with cell morphologies. Additionally, small silicate botryoids (2 to <0.5 μm ; e.g., PAJ-2.1 incubation

in Figure 10C), likely opal, and globular grains of magnesium-rich silicate composition, likely proto-phyllsilicate phases, were observed (e.g., PAJ-15 incubation in Figure 10D).

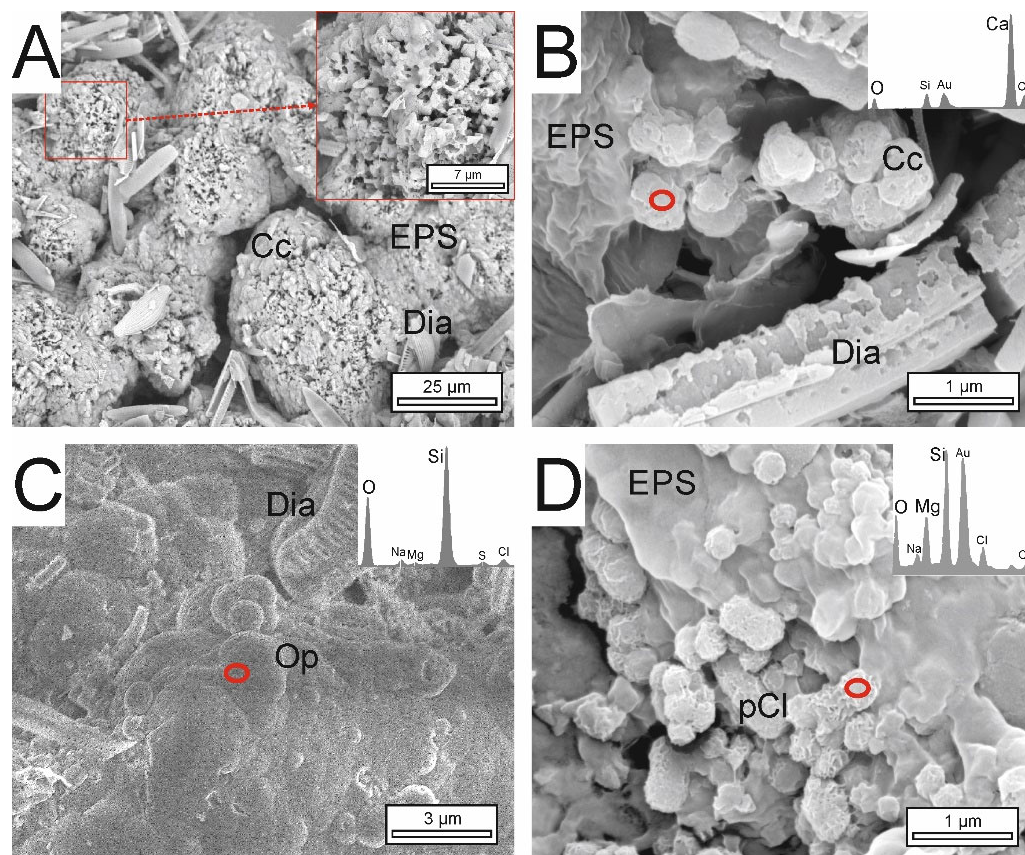


Figure 10. New minerals identified in the following field emission scanning electron microscope (FE-SEM) checkups after two months of running microcosms. All of them correspond to Salar de Pajonales incubations. (A) Highly porous calcite crystals (Cc) surrounded by dispersed *Amphora* frustules (Dia) from the PAJ-10 incubation. Zoomed view of a single crystal at the right side. (B) Calcitic grains emerging from denatured extracellular polymeric substances (EPS) enclosed by partially dissolved diatom frustules (Dia) from the PAJ-15 incubation. Spot (red circle) EDX shows Si enrichment. (C) Botryoidal opal aggregates (Op) near *Amphora* frustules (Dia) from the PAJ-2.1 incubation. Spot (red circle) EDX spectra in the upper right. (D) PAJ-15 incubation showing similar grains as in (B) emerging from a glutinous EPS. In contrast to (B), spot (red circle) EDX confirmed magnesium silicate composition of proto-phyllsilicate minerals (proto clay-pCl). Note the internal nanometric fiber-like structure.

Abiotic precipitates were observed after 90 days as prismatic gypsum crystals up to 0.5 mm in size (Figure 11A) in the control without a microbial mat that was allowed to evaporate (CGOR-1, Supplementary Table S1). These crystals showed very sharp edges (Figure 11B,C). Euhedral crystals of halite and sylvite were observed thereafter (not shown). No unevaporated control had precipitates (CGOR-2 to CGOR-19 and CPAJ-1 to CPAJ-7), and the evaporated control (CGOR-1) did not show different minerals through the rest of the experiment.

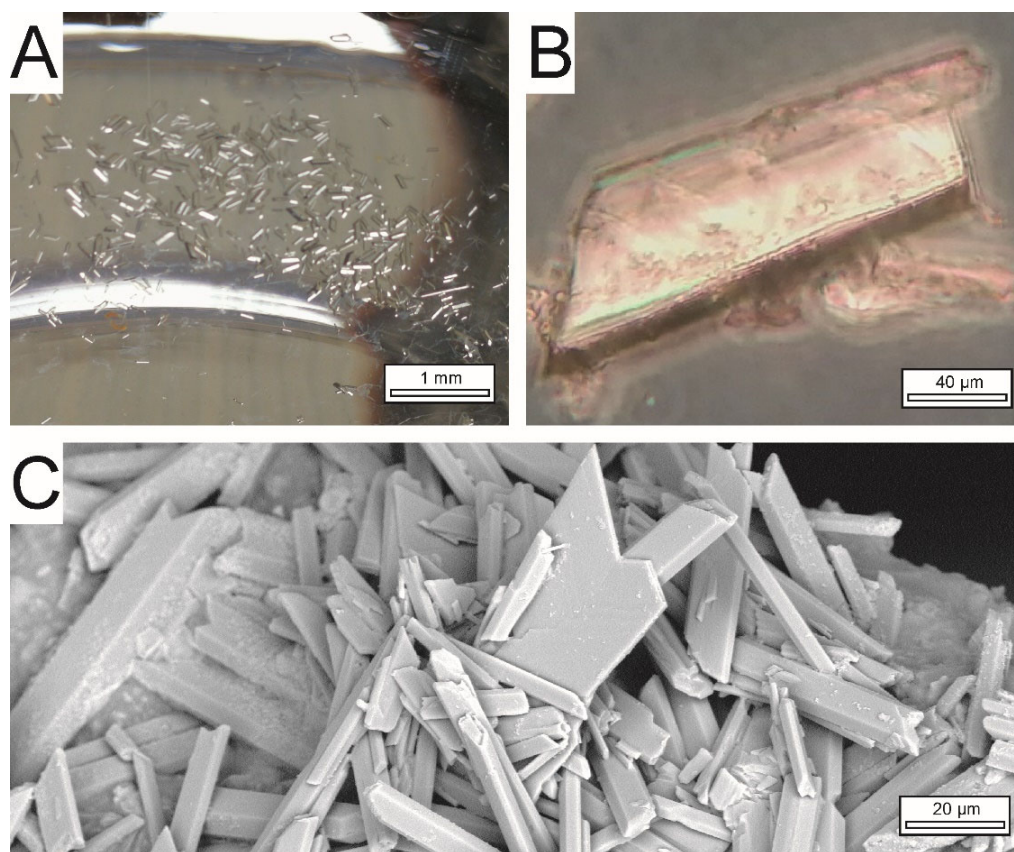


Figure 11. A photograph (A) and two photomicrographs (B,C) of abiotic crystals obtained from the evaporation control (CGOR-1) at different scales: (A) macro view of the transparent gypsum crystals in its precipitation solution under glass and micro views of optical microscopy (B) and FE-SEM (C). Crystals are c-axis-elongated with very sharp edges. Some of them are fishtail-twinned in (C).

4. Discussion

These experimental microcosms allowed us to monitor changes to the whole microbial mat as a system over time. The macroscopic structure of the mats was characterized, and some groups of bigger micro-organisms (cyanobacteria, diatoms, and sulfur-oxidizing bacteria, among others) were identified but not isolated. The physicochemistry and mineralogy also evolved through time, so they were evaluated over the course of the experimental period.

Microcosms are not widely used to test natural environments, except for specific applications, for instance, soil and crop management, as in [62], and biomining in simulated gravity [63], among others. In fact, microcosms with microbial mats, such as those presented in our study, are scarce. Only a few studies of microcosms running environmental microbial mat experiments can be found in the literature (i.e., to follow anaerobic degradation of organic matter in tidal flat sediments in [64]; development of bacterial and archaeal communities at different salinities in [65], as most other studies are focused on specific applications (i.e., oil degradation in [66]).

The use of environmental conditions that simulate the natural system applied to complete mats, together with controls, differentiates the methods presented here from more common microbiological methods (isolates and enriched cultures) to induce biotic precipitation of minerals. Unlike the experiments with isolated cultures, these all-in-one experiments are not common because they do not provide a simple way to link mineral precipitation to either a specific organism or a specific metabolism [16,17]. Besides that, the pathway of formation of many minerals is still widely discussed, probably because the processes of their formation are slow (e.g., dolomite, [27,30]) or involve many different types of microbial interactions (various microbial metabolisms and different organic

substances). Therefore, experiments such as the one presented here could be useful in simulating the precipitation of dolomite-group minerals or other phases that may require more time to form. These phases could originate in the mat from the interactions of a consortium of micro-organisms and even from the action of slower organic processes, such as degradation of complex organic molecules [16,30]. Similarly, these experiments are useful in elucidating the precipitation of phases with more complex kinetics (e.g., double salts). Without further experimentation, it will remain unclear which of the proposed mechanisms (e.g., degradation) or a combination of the various metabolic functions of the consortium is relevant to mineral precipitation in the presence of micro-organisms. Finally, microcosm experiments can be considered a step forward in the development of more specific experiments [67–74], although most of previous studies did not focus on the substrate and/or mineral precipitation.

The amount of time and resources invested in conducting specific experiments that are not always reproducible is widely known (e.g., [75]), so more methods to simulate the environment, such as microcosms, are necessary, specifically for mineral precipitation associated with mat-forming micro-organisms. Microcosms of forcing conditions are currently being addressed for the precipitation of minerals [76].

Physicochemical evaluations over time are important to monitor the chemical stability of the environment, as well as the heterogeneity of the systems in which the microbial mats grow and where the minerals precipitate [55]. Changes or stability of pH and salinity values can be understood as microbial activity or precipitation processes occurring within the incubations, although not all of them. For instance, higher fluctuations of salinity and pH were observed in PAJ than in GOR samples, including their respective water-only controls, which can be attributed to higher-salinity brines of PAJ (Figure 4). Brines of higher salinity varied, increasingly affected, by seasonal changes (humidity, temperature) in the microcosm chamber (e.g., Supplementary Figure S6).

Only a few studies have monitored mats through time [17,55,73,74,76]. Studies of seasonal mats in Spanish lakes showed similarities with mats from Chilean salt flats; for instance, diatoms and cyanobacterial cells quickly bloomed, but end development in thickness and macroscopic texture seemed to differ. Incubations from PAJ developed thicker microbial mats than those from GOR in shorter times, presumably because acidic media limited the growth of GOR mats, as suggested by Escudero et al. [50].

We defined ‘mat stabilization’ as the early period during which some micro-organisms bloomed, elevating some mat functions; for instance, phototrophic activities of the mat may be temporarily increased due to diatom blooming in the first days, and this can affect the water column of the incubations, elevating pH (CO₂ uptake). Salinity and pH fluctuated considerably in the first days for most incubations, compared to slighter changes of these parameters through the rest of the experiment (Figure 4). Salinity changes were more evident in experiments with substrates and showed a higher rate with fine than with coarse gypsum, suggesting that the substrate and even mat dissolution could play a role in that increase (e.g., Supplementary Figure S3). During this period, the mat is ‘unstable’ as it is acclimated to the laboratory conditions. Changes in pH could be attributed to micro-organism’s acclimation, as environmental conditions in nature fluctuate more than in the laboratory (e.g., day/night or seasonal changes). The stabilization period in our microbial mats took between 30 and 100 days, as shown by more prominent changes in pH and salinity compared to >100-day values (Figure 4). Osman et al. [74] reported results of similar microcosms experiments, showing that such changes should not greatly impact the diversity of the community—the abundance of each micro-organism in the community. Therefore, it can be inferred as a lapse of time when the microbial community reorganizes. Their results were obtained by comparing living field and laboratory cultures of stromatolites from a similar environment, the hypersaline Laguna Interna. After the stabilization period, the mat remains ‘stabilized’ in a continuous growth without blooms promoted by the biomass generators of the community (phototrophs), with only small seasonal changes, as previously reported [17], in cases with no evaporation. Depending

on the nature of the substrate in stagnant incubations, such as ours, depletion of nutrients or water recirculation, as in Osman et al. [74], would determine mat growth in the long term. Our observations suggest that microbial mats can continue to grow biomass based on natural substrates and brine, and maintain a community for a long period (more than 300 days, as in Figure 6M), even if the brine is stagnant.

Massive precipitation of supersaturated phases, such as carbonates, which are usually supersaturated in saline brines [15–17], would have resulted in brine changes and coprecipitation or dissolution of other phases. In an evaporative scenario, abiotic precipitation of supersaturated salts may also occur. However, these two cases were not detected in our experiments, as sudden pH or salinity changes were not observed during monitoring (Figure 4C, Supplementary Figures S1–S13). In fact, the salinity changes observed in PAJ and GOR incubations were minor (Figure 4A,C), and major pH changes (Figure 4B,D) can be attributed mostly to acclimatation. This was more noticeable for PAJ incubations, as pH fluctuated considerably between 0 and approximately 100 days and then remained more stable. In addition, these physicochemical changes and the calculated supersaturation state of the minerals of modeled brines did not correlate with the minerals that are predicted to precipitate abiotically in controls (e.g., calcite). For instance, calcite, which was supersaturated in all PAJ brines, and gypsum and halite, which were supersaturated in the most concentrated brines of PAJ and GOR (e.g., PAJ-7 brine, Table 1), did not precipitate in the respective brine controls (without microbial mats under non-evaporative conditions). Lastly, pH increased for both controls and microbial mat samples in the 100 to 330-day period, as well as from day 330 to the end of the experimental period in microbial mat samples, whereas it decreased in controls during the same period (Figure 4B,D; Supplementary Figure S1). This suggests that pH behavior of the water column diverges through time when comparing non-evaporated controls to mat samples due to microbial activity and/or mineral precipitation within the mats (Supplementary Figure S1, Supplementary Table S1). In addition, salinity exhibited opposite behavior from day 330 to the end of the experimental period, suggesting an inverse link between salinity and pH (Figure 4B,D; Supplementary Figure S1).

Microbial presence was crucial for the precipitation of the minerals in our experiments, as it affected pH and salinity values throughout the experimental period. As an example, after 100 days, most PAJ samples with no substrate (Supplementary Figures S1–S9) and those with fine and coarse gypsum substrates slightly diminished and maintained their salinity during the experiment in comparison with water-only controls, these on which salinity slightly increased over time (Figure 4). Conversely, pH increased when microbial mats were present compared to the controls without microbial mats, on which pH fluctuated, regardless of the presence of a gypsum substrate; therefore, the increase in pH can be attributed to microbial activity. In addition, larger changes in salinity and pH were observed for GOR incubations compared to controls without mats (Supplementary Figures S10–S13), with even larger changes compared to incubations wherein mats grew in substrates (Figure 4).

The laboratory experiments presented here can be compared to the results obtained from field studies for better understanding of natural processes. We think that the acquired knowledge may provide insights for the design of future experiments under controlled conditions. Additionally, incubations of microbial mats in laboratory microcosms can serve as the starting point to study unculturable microbes (for instance, by finding a workaround for isolation). Improving our understanding of natural processes could lead to replication of mineral paragenesis and synthesis of minerals similar to that found in nature [76].

4.1. Substrates Used in Microcosms

The experiments with microbial mats in the presence and absence of substrates presented here evidence that natural substrates enhance microbial growth and mat (biomass) development (e.g., Supplementary Figure S14). One of the main advantages of using substrates in laboratory experiments or microcosms is that they serve as a support for

microbial attachment. In our case, the substrate was shown to play a role in microbial mat growth. This was noticeable through direct observation (Supplementary Figure S14) and PCO (Figure 5), as the third group was formed by microbial mats without a substrate, which suggests that the other two groups differentiated due to the substrate. Therefore, microbial mats can grow, developing thick layers, resulting in precipitation that can be easily observed and analyzed by the presented techniques in our study. In addition, microbial mat growth can be used as a biomass source for many other purposes, as microbial mats condense EPS, e.g., for lithification [7,77].

A second discussion point is relevant when selecting the substrate to be used. There are some examples in the literature in which micro-organisms were grown using different substrates. For instance, it is quite common to use agar (e.g., Popall et al. [78]). Other authors have used natural boulders [73], <3 cm glass beads [69], aquarium sand [73,74], pure quartz sand [72,79,80], siliciclastic beach sand [71], and wells of carbonate-coated microfluidic chips [81], among other substrate materials. Most of the substrates used for research are artificial; however, the use of natural substrates can help to replicate some of the environmental conditions of the sites where the original micro-organisms were growing. This could improve scientific results because the presence of environmental nutrients could enhance growth, and substrate surfaces could favor attachment. On one hand, micro-organisms are adapted to natural substrate surfaces; therefore, these substrates may help them attach or may speed up attachment, developing thicker and healthier mats (for instance, as can be seen in Supplementary Figure S14 when comparing different gypsum substrates and no substrate in PAJ-7.1 to PAJ-7.3 incubations). On the other hand, a natural substrate provides the communities with nutrients that are present in their natural environments, even if the substrate has been processed through morphological changes or subjected to autoclaved sterilization. Therefore, by adding foreign but natural substrates, micro-organisms in the mats can obtain their natural nutrients by a variety of mechanisms [7]. For instance, cyanobacteria, diatoms, and heterotrophic bacteria can dissolve silica in a carbonate-rich environment by locally elevating pH [82,83]. This could explain the abnormal abundance of eukaryotes reported in microbialite aquarium experiments conducted by Couradeau et al. [70] and could also explain the diatom blooms observed in our experiments during 'mat stabilization', as our containers were also made of glass. Additionally, adding an artificial substrate and/or removing the natural substrate could lead to increased community stress, forcing the mats to produce EPS and therefore changing the precipitation pathways. In this direction, Osman et al. [74] compared the mineralogy of a commercial substrate with that of a microbialite and found that they were substantially different. They also compared the microbial diversity of a natural mat in the field with that of a mat incubated in the laboratory based on its natural microbialitic substrate, showing that the abundance of each microbial group was similar between the two samples. It has been reported that small changes in microbial diversity can substantially change the activity of micro-organisms and biomass production [84]. Therefore, experiments with commercial substrates can be successful, specifically to reproduce some simple marine substrates; however, complex sediments of continental environments can hinder their success, for instance, in terms of mineralogy. Finally, the grain size affects experimental outcomes. Guerrero et al. [85] evaluated the absence or presence of mats attached to particle substrates of different sizes in natural environments. They concluded that the attachment to different substrates depends on the main organisms forming the mat and not on the grain size. In our case, fine gypsum substrates helped communities to develop thicker mats in PAJ (Figure S14, Supplementary Material) in comparison with coarse gypsum substrates, so it seems that communities preferred to grow in fine detrital gypsum sand. In summary, substrates obtained from a natural source and then treated, as in this study, were found to be an alternative with achieving good mineralogical results [68].

4.2. Monitoring Communities: Short-Term and Long-Term Mineral Formation Implications

Gypsum of various morphologies was the main phase that precipitated within microbial mat incubations (Figure 9). Many studies point out that the organic molecules present in microbial mats are inhibitors in the formation of gypsum because they retard nucleation and/or growth [3,86–89]. This happens because organic molecules either act as binders of ions or they are attracted to the faces where ions would accumulate during crystal growth [90,91]. However, the gypsum formation in the microbial mats observed in this study supports results of other recent studies showing that the destabilization of organic molecules by factors such as decomposition favors gypsum nucleation and growth [16,19] in biologically influenced mineralization processes [92]. Indeed, most of the microbial-mat incubations did not produce perfectly prismatic crystals with morphology compatible with pure abiotic precipitation, as observed by comparing the crystals formed in the evaporated control (CGOR-1, Supplementary Table S1; Figure 11) with those formed in the PAJ-11 mat incubation (Figure 9B). Non-prismatic textures are known to be exclusive to organic media due to the distinct affinities to adsorb onto specific crystal surfaces [3]. Therefore, some events, for example, the degradation of the EPS, favor nucleation and growth. Indeed, certain organic monolayers can accelerate gypsum nucleation rates [93,94] to a degree that seems to correlate with the calcium-binding capacities of those layers [94]. Moreover, such monolayers can also induce specific crystallographic orientations of gypsum crystals growing on these templates [93], explaining the presence of the morphologies precipitated within the mats (e.g., Figure 9A–F). Therefore, the prismatic crystals shown in Figure 9B,C may have nucleated as a result of being triggered by organics, growing partially outside the EPS, whereas all other crystals (Figure 9A,D–F) may have been formed completely inside organic gels.

Halite has always been considered an abiotic evaporite, as it can easily precipitate from most $\text{Na}^+\text{-Cl}^-$ -rich brines without the help of micro-organisms, and most research has focused on microbes inhabiting within this mineral (e.g., Wierzbos et al. [95]). In our opinion, it is not yet clear how microbes can affect the precipitation of halite; however, according to our results, similar biologically influenced processes [92] as those described for gypsum [3] may have taken place for halite. The prismatic crystals (Figure 9G,H) may have nucleated in the EPS but became euhedral outside the EPS as the organic matter was degraded through time. In addition, the presence of organic matter embedding crystals may have resulted in subhedral to anhedral halite crystals (Figure 9I).

Spherulitic silicates, carbonates, and proto-phyllsilicates (proto-clay) minerals were observed in microbial mat incubations (e.g., PAJ-10 and PAJ-15) after the early appearance of gypsum and halite (Figure 10). Silica spherules have been widely reported to precipitate abiotically as a result of pH changes in geothermal environments, and biotically forming stromatolites in other settings worldwide, e.g., hot springs [96] and caves [97]. In our microcosms, microbes may have played a role in silicate precipitation. On one hand, fluid cooling did not occur in our case, and intense bubbling may have led to important pH changes. However, in our microbial mats, we observed only mild bubbling, and physicochemical monitoring indicated slight pH changes during silicate precipitation (Figs. 4, 10). On the other hand, we observed diatoms elsewhere, and silicates found in diatoms and sponges have recently received research attention in minerals with a biological origin [96,97]. Some novel research has been conducted to show how proteins can control the precipitation of biosilica composites inside cells [98]. Specifically, the protein lysozyme interacts with the polymerizing silica during nucleation, particle growth, and aggregation by electrostatic and hydrophobic mechanisms, resulting in hybrid structures of nanosphere aggregates, most of them highly amorphous. The destabilization of these biosilica composites due to cell death and/or their EPS denaturation enhances concentration locally and therefore facilitates precipitation and aggregation as the triggering mechanism of our silicate botryoids (Figure 10C). Additionally, recent experiments demonstrated that biomediated silica spherules require the presence of extracellular polymeric substances (EPS), photosynthetically induced pH changes, magnesium cations (Mg^{2+}), and >70 ppm

silica [31,81]. A combination of biologically induced and influenced processes summarized for carbonates in Konhauser [99], pp. 160–166, and Dupraz et al. [92] from different molecules through different mechanisms (i.e., negatively charged electrostatic attachment and positively charged hydrophobic interactions) may be applied to the silicates in our case. However, the diatoms case is not yet understood, so biomimetic studies focusing on the mechanism of interaction between organic molecules and silica are still needed [96].

Calcium carbonates are probably the most studied group of minerals from a microbially (or organically) mediated point of view, with calcite being the most abundant. Consequently, we know of many pathways to precipitate calcite, and these were summarized by Dupraz et al. [92]. It is widely accepted that stromatolites are microbially mediated carbonate rocks, and environmental research has shown that precipitation takes place only inside the microbial mat [7,27,100], even if the water column is supersaturated with respect to carbonates [15,17,28]. Furthermore, there is increasing evidence that several microbial metabolisms can lead to the formation of carbonate microbialites, as well as in EPS templates [7,27–30]. The cell wall of bacteria and the frequently associated EPS are typically rich in anionic functional groups, which tend to scavenge metal ions (e.g., Ca^{2+}) from the surrounding solution and may create a local environment with increased ion concentration. Our results suggest that the calcite seen in Figure 10A could be precipitated in an EPS-rich microbial matrix, which showed pores of bacterial external molds and microbial remains. These microbial imprints are similar to the morphologies observed in other calcite precipitates (Figure 9I–L in Marin et al. [77]). In the mentioned study, precipitation of calcite was induced by heterotrophic metabolism and organic matter decay.

Small (<1 μm) spherules of calcium carbonate and magnesium silicate were seen precipitating within the EPS (Figure 10B,D). Globular morphology reminiscent of cells suggests that precipitates coated the exterior of the cell wall (as in Moore et al. [81]), but the detailed view of the spherules, which have needles protruding from their interiors, points to a process in which ions are expelled as the cells die and they and their EPS degrade. Consequently, a similar morphology with different composition (Ca-carbonate or Mg-silicate) can result, depending on which ions are expelled, which in turn depends on the cell/EPS chemical composition, i.e., enriched in Si in the case of diatom EPS. Si-enriched organics coating minerals are likely the reason for the presence of Si in Ca-carbonate spectra (Figure 10B). Note that frustule dissolution may require an alkaline pH of 9 or 10 [82,83], which was never reached in the water column, so there had to be compatible microenvironments raising to favor calcite precipitation.

In the case of Ca-carbonates, spherules are commonly found in nature [92], but spherules of Mg-silicates are scarce. A few recent experiments showed similar spherules in cyanobacterial cultures and enrichments [31,81]. Assuming that these Mg-silicates are metastable intermediate-phase precursors of clays, such as sepiolite or kerolite ($(\text{Mg},\text{Ni})_3\text{Si}_4\text{O}_{10}(\text{OH})_2\cdot\text{H}_2\text{O}$), we compared morphologies from previous studies and discussed the proposed pathways of formation for the origin of these clays. Sepiolite fiber-like morphologies of different sizes observed in microphotographs (e.g., Pozo and Calvo [101]; del Buey et al. [18]; Martín-Perez et al. [102]) do not perfectly match those observed in our experiments. Although it is possible that the EPS that obscures the needles in the spherules prevents us from distinguishing fiber-like morphologies inside the spherules (Figure 10D), Mg-clay minerals have different morphologies [101], which could explain why we did not observe needle-like morphology in our experiments. In addition, the mechanism proposed by del Buey et al. [19] to form Mg-silicates by expelling ions derived from EPS dehydration could apply here, as degradation can also expel ions. This would complement the precipitation pathway from colloidal solutions summarized by Pozo and Calvo [101]. In addition, kerolite formation was recently reported in a cave associated with fossil organic matter [102]. If kerolite is genetically related to the fossil organic matter in the abovementioned cave, its formation may have required an organic/amorphous template rich in magnesium and silica to precipitate, as in other scenarios occur [18,19,31,81]. EPS can play a similar role as a template, and non-degraded organics can partially fossilize later during diagenesis; therefore, this origin could be applied in our biotic scenario [31,80,81].

4.3. Textures for the Interpretation of Recent and Preserved Microbialites

Salt flats contain abundant microbialitic/thrombolytic/stromatolitic structures of layered gypsum and/or halite that share several common features with carbonate microbialites [3,17,20,21,23,37,103], although a general model of their formation has not yet been proposed [3]. The lack of such a model enhances the interest in gypsum microbialite research because their characterization is of utmost importance to correctly model the burial rate of sulfates when considering the sulfur cycle [3]. Until now, a certain agreement existed about the notion that (cyclic) wide fluctuations in water salinity, due to seasonal and/or long-term variations in the ratio of water inflow and evaporation rate, coupled to changes in water depth, stratification, and circulation may have originated these laminated and domal structures, specifically for gypsum (e.g., [2], p. 225, [48,104]). Besides that, other studies reported the involvement of microbial mats in the formation of these structures in modern (e.g., [12,21,22]) and older systems [105–107]. In addition, some authors agreed that in modern environments, gas accumulation below microbial mats may be the origin of some domical structures, which can be preserved (e.g., [21,23]). In our experiments, the evolution of incubations suggested that microbes may play a role in the formation of these structures (e.g., lamination of gypsum in Figure 6E) and the domal structures (not shown) apparently without the wide environmental salinity fluctuations (Figure 4). Therefore, we are aware that micro-organisms can produce these mineral laminations that become lithified, although complex growing mechanisms that were inferred cannot completely be assessed by our observations. In our opinion, gas produced by the microbial metabolisms (Figure 6I) and trapped below the biofilms (Figure 6E,M) may initiate the formation of the smaller domical microstructures observed in PAJ and GOR, which is in agreement with the conclusions of Farias et al. [21] and Ercilla Herrero [23]. Seasonal variations and further mineralization of these structures over time could result in an amplification to centimeters-wide domical macrostructures. The study of these structures is in progress, and some textural features pointing to this direction have been preliminarily published [53].

The appearance of silicates in our experiments has started a discussion on the need to determine their origin. Microbially mediated or not, the silicification process is known to aid in the preservation of early sedimentary structures and microbial mat textures in Precambrian rocks, as some experiments have demonstrated, if it occurs at the correct time [31,81,108,109]. In addition, silicification can help to preserve primary textures of carbonates, sulphates, and halides, as these can be mimetically (sometimes sequentially) replaced during silicification of recent sediments [108]. The textures of the silicates obtained in our experiments (e.g., botryoids, as in Figure 10C) are similar to those shown in Moore et al. [31,81] experiments. Additionally, our microcosms also produced similar paragenesis of sulphates, halides, and carbonates that as those discussed in these studies. Therefore, our geochemical results provide environmental constraints, and our petrographic results could aid in the interpretation of textures of minerals and organics in old rocks to advance knowledge of Early Earth.

5. Conclusions

Our microcosm experiments showed the possibility of forming evaporite mineral phases in the absence of evaporation. Therefore, although evaporation has traditionally been considered the main and only mineral-forming mechanism in salt flat environments, our work suggests that it is not an essential requirement for rock-forming paragenesis in the fossil record. More research on evaporites and, specifically, more experimental research with natural samples, is necessary to differentiate biotic and abiotic participation in the chemistry of these processes. These processes, which generate macroscale and microscale mineral deposits and textures, and which are used to search for extraterrestrial life, among other applications.

The supersaturation state of minerals calculated through classical geochemical modeling using environmental parameters measured in the field or obtained in the laboratory is

not necessarily representative of the minerals precipitating from a given brine. As reflected in controls, it is just an abiotic prediction.

Natural substrates with similar compositions (i.e., mimicking chemistry and/or using the same source) worked successfully to grow natural microbial mats in our microcosm experiments. Mat-supporting substrates based on natural environments can be used to design experiments in similar and different environments (after appropriate modifications, e.g., substrate chemistry or grain size). Similarities and differences among the fabrics and paragenesis of the minerals reported here could help to interpret biologically induced or influenced minerals in other environments (i.e., caves, tidal flats, and open marine environments, outside world's condition imitations, among others).

Supplementary Materials: The following supporting information can be downloaded at: <https://www.mdpi.com/article/10.3390/min12050646/s1>, Table S1: Summary of the microbial mats observations and minerals precipitated within the experiments; Figure S1: Physicochemistry of Salar de Pajonales (A,B) and Salar de Gorbea incubations (C,D); Figure S2: Water column fluctuations of salinity measurements in Salar de Pajonales incubations corresponding to PAJ-6.1 (fine gypsum substrate), PAJ 6.2 (no substrate), and CPAJ-6 (control); Figure S3: Water column fluctuations of salinity measurements in Salar de Pajonales incubations corresponding to PAJ-7.1 (fine gypsum substrate), PAJ-7.2 (no substrate), PAJ-7.3 (coarse gypsum substrate) and CPAJ-7 (water-only control); Figure S4: Water column fluctuations of salinity measurements in Salar de Pajonales incubations corresponding to PAJ-16 (fine gypsum substrate), PAJ 12 and PAJ-17 (no substrate), and CPAJ-7 (control); Figure S5: Water column fluctuations of salinity measurements in Salar de Pajonales incubations corresponding to PAJ-2.1 (fine gypsum substrate), PAJ-2.2, PAJ-10, PAJ-11, PAJ-14, PAJ-15, (no substrate), PAJ-1 (coarse gypsum substrate) and CPAJ-1 (control); Figure S6: Water column fluctuations of salinity measurements in Salar de Pajonales incubations corresponding to PAJ-5.1 (fine gypsum substrate), PAJ-4.1 and PAJ-5.2 (no substrate), PAJ-3, PAJ-4.2, PAJ-13 (coarse gypsum substrate) and CPAJ-4 (control); Figure S7: Water column fluctuations of pH measurements in Salar de Pajonales incubations corresponding to PAJ-16 (fine gypsum substrate), PAJ-10, PAJ-11, PAJ-12, PAJ-14, PAJ-15, PAJ-17 (no substrate), PAJ-13 (coarse gypsum substrate) and CPAJ-7 (control); Figure S8: Water column fluctuations of pH measurements in Salar de Pajonales incubations corresponding to PAJ-6.1 and PAJ-7.1 (fine gypsum substrate), PAJ-6.2 and PAJ-7.2 (no substrate), PAJ-7.3 (coarse gypsum substrate) and CPAJ-6 and CPAJ-7 (control); Figure S9: Water column fluctuations of pH measurements in Salar de Pajonales incubations corresponding to PAJ-2.1 and PAJ-5-1 (fine gypsum substrate), PAJ-2.2, PAJ-4.2, PAJ-5.2 (no substrate), PAJ-1, PAJ-3 and PAJ-4.2 (coarse gypsum substrate) and CPAJ-1 and CPA-4(control); Figure S10: Water column fluctuations of salinity measurements in Salar de Gorbea incubations corresponding to GOR-10, GOR-14, GOR-15, GOR-16, GOR-18.2, GOR-19 (no substrate), GOR-1, GOR-17, GOR-18.1 (coarse gypsum substrate) and CGOR-10, CGOR-14, CGOR-15, CGOR-16, CGOR-17, CGOR-19 (control); Figure S11: Water column fluctuations of salinity measurements in Salar de Gorbea incubations corresponding to GOR-11, GOR-12, GOR-13, (no substrate), GOR-2 (coarse gypsum substrate) and CGOR-2, CGOR-11, CGOR-12, CGOR-13 (control); Figure S12: Water column fluctuations of pH measurements in Salar de Gorbea incubations corresponding to all samples except GOR-2; Figure S13: Water column fluctuations of pH measurements in Salar de Gorbea incubations corresponding to GOR-2 (coarse gypsum substrate), and CGOR-2 (control). GOR-2 greatly increased pH up to 85 days, and then it fluctuated; Figure S14: Side (left photographs) and top views (right photographs) of no substrate PAJ-7.2 (A), fine gypsum substrate PAJ-7.1 (B), and coarse gypsum substrate PAJ-7.3 (C) incubations from 0 days (upper photographs) to 136 days (lower photographs). The sample without substrate (PAJ-7.2) did not show microbial mat growth; Figure S15: Bright light microphotographs of a microbial mat with diatoms (Dia) embedded in extracellular polymeric substances (EPS) including prismatic (pGp) and lenticular (lGp) gypsum crystals before purification (A) and after purification without crystals (B).

Author Contributions: Ó.C. supervised the project, aided by C.D., and wrote the manuscript, aided by C.T.-C., C.D., N.W.H. considerably improved the manuscript with revisions and suggestions. Ó.C., C.T.-C., C.D. and N.W.H. carried out field trips. Ó.C. and C.T.-C. designed and ran the microcosm experiment under the supervision of C.D. Ó.C. and C.T.-C. sampled and monitored the experiment, obtained results, and interpreted them. C.T.-C. carried out the simulations in PHREEQC

and processed data in Primer6. Ó.C. drafted the figures, aided by C.T.-C. All authors have read and agreed to the published version of the manuscript.

Funding: “Proyecto CONICYT Postdoctorado 3190821” and “Beca CONICYT Doctorado Nacional 21181422”. “Proyecto 32002137 Minera Escondida Limited” and NASA Astrobiology Institute (NAI) via grant no. The NNA15BB01A (N. A. Cabrol, PI) project that allowed us to collect some of the samples and make observations.

Data Availability Statement: The data presented in this study are available in Supplementary Material.

Acknowledgments: The authors are appreciative of the support of the staff at MAINI and CBAR laboratory facilities, Universidad Católica del Norte, Antofagasta, Chile. Thanks to Pieter T. Visscher and M. Esther Sanz-Montero for sharing ideas that triggered these experiments and results, as well as Carlos Pedrós Alió for his advice and guidance with respect to organizing the results.

Conflicts of Interest: The authors declare no conflict of interest.

References

1. Eugster, H.P.; Hardie, L.A. Saline Lakes. In *Physics and Chemistry of Lakes*; Lerman, A., Ed.; Springer: Berlin/Heidelberg, Germany, 1978; pp. 237–293.
2. Warren, J.K. *Evaporites: Sediments, Sources and Hydrocarbons*; Springer: Berlin, Germany, 2006; 1035p.
3. Van Driessche AE, S.; Stawski, T.M.; Kellermeier, M. Calcium sulfate precipitation pathways in natural and engineered environments. *Chem. Geol.* **2019**, *530*, 119274. [[CrossRef](#)]
4. Cabrol, N.A.; McKay, C.P.; Grin, E.A.; Kiss, K.T.; Ács, É.; Tóth, B.; Grigorszky, I.; Szabó-Taylor, K.; Fike, D.A.; Hock, A.N.; et al. Signatures of habitats and life in Earth’s high-altitude lakes: Clues to Noachian aqueous environments on Mars. In *The Geology of Mars: Evidence from Earth-Based Analogs*; Cambridge University Press: Cambridge, UK, 2009.
5. Newman, D.K.; Banfield, J.F. Geomicrobiology: How molecular-scale interactions underpin biogeochemical systems. *Science* **2002**, *296*, 1071–1077. [[CrossRef](#)] [[PubMed](#)]
6. Montague, C.L. Influence of biota on erodibility of sediments. In *Estuarine Cohesive Sediment Dynamics*; Springer: New York, NY, USA, 1986; pp. 251–269.
7. Dupraz, C.; Visscher, P.T. Microbial lithification in marine stromatolites and hypersaline mats. *Trends Microbiol.* **2005**, *13*, 429–438. [[CrossRef](#)] [[PubMed](#)]
8. Jones, B.E.; Grant, W.D.; Duckworth, A.W.; Owenson, G.G. Microbial diversity of soda lakes. *Extremophiles* **1998**, *2*, 191–200. [[CrossRef](#)] [[PubMed](#)]
9. Burne, R.V.; Moore, L.S. Microbialites; organosedimentary deposits of benthic microbial communities. *Palaios* **1987**, *2*, 241–254. [[CrossRef](#)]
10. Kobluk, D.R.; Crawford, D.R. A modern hypersaline organic mud-and gypsum-dominated basin and associated microbialites. *Palaios* **1990**, *5*, 134–148. [[CrossRef](#)]
11. Vogel, M.B.; Des Marais, D.J.; Parenteau, M.N.; Jahnke, L.L.; Turk, K.A.; Kubo, M.D. Biological influences on modern sulfates: Textures and composition of gypsum deposits from Guerrero Negro, Baja California Sur, Mexico. *Sediment. Geol.* **2010**, *223*, 265–280. [[CrossRef](#)]
12. Petrash, D.A.; Gingras, M.K.; Lalonde, S.V.; Orange, F.; Pecoits, E.; Konhauser, K.O. Dynamic controls on accretion and lithification of modern gypsum-dominated thrombolites, Los Roques, Venezuela. *Sediment. Geol.* **2012**, *245*, 29–47. [[CrossRef](#)]
13. Taher, A.G. Microbially induced sedimentary structures in evaporite–siliciclastic sediments of Ras Gemsa sabkha, Red Sea Coast, Egypt. *J. Adv. Res.* **2014**, *5*, 577–586. [[CrossRef](#)]
14. Strohmenger, C.J.; Jameson, J. Gypsum stromatolites from Sawda Nathil: Relicts from a southern coastline of Qatar. *Carbonates Evaporites* **2018**, *33*, 169–186. [[CrossRef](#)]
15. Cabestrero, Ó.; Sanz-Montero, M.E. Brine evolution in two inland evaporative environments: Influence of microbial mats in mineral precipitation. *J. Paleolimnol.* **2016**, *59*, 139–157. [[CrossRef](#)]
16. Cabestrero, Ó.; del Buey, P.; Sanz-Montero, M.E. Biosedimentary and geochemical constraints on the precipitation of mineral crusts in shallow sulphate lakes. *Sediment. Geol.* **2018**, *366*, 32–46. [[CrossRef](#)]
17. Cabestrero, Ó.; Sanz-Montero, M.E.; Arregui, L.; Serrano, S.; Visscher, P.T. Seasonal variability of mineral formation in microbial mats subjected to drying and wetting cycles in alkaline and hypersaline sedimentary environments. *Aquat. Geochem.* **2018**, *24*, 79–105. [[CrossRef](#)]
18. del Buey, P.; Cabestrero, Ó.; Arroyo, X.; Sanz-Montero, M.E. Microbially induced palygorskite-sepiolite authigenesis in modern hypersaline lakes (Central Spain). *Appl. Clay Sci.* **2018**, *160*, 9–21. [[CrossRef](#)]
19. del Buey, P.; Sanz-Montero, M.E.; Braissant, O.; Cabestrero, Ó.; Visscher, P.T. The role of microbial extracellular polymeric substances on formation of sulfate minerals and fibrous Mg-clays. *Chem. Geol.* **2021**, *581*, 120403. [[CrossRef](#)]
20. Demergasso, C.; Chong, G.; Galleguillos, P.; Escudero, L.; Martínez-Alonso, M.; Esteve, I. Tapetes microbianos del Salar de Lllamará, norte de Chile. *Rev. Chil. Hist. Nat.* **2003**, *76*, 485–499. [[CrossRef](#)]

21. Farias, M.E.; Contreras, M.; Rasuk, M.C.; Kurth, D.; Flores, M.R.; Poire, D.G.; Novoa, F.; Visscher, P.T. Characterization of bacterial diversity associated with microbial mats, gypsum evaporites and carbonate microbialites in thalassic wetlands: Tebenquiche and La Brava, Salar de Atacama, Chile. *Extremophiles* **2014**, *18*, 311–329. [[CrossRef](#)]
22. Rasuk, M.C.; Kurth, D.; Flores, M.R.; Contreras, M.; Novoa, F.; Poire, D.; Farias, M.E. Microbial characterization of microbial ecosystems associated to evaporites domes of gypsum in Salar de Llamara in Atacama Desert. *Microb. Ecol.* **2014**, *68*, 483–494. [[CrossRef](#)]
23. Ercilla Herrero, O. Origen y evolución de estromatolitos de yeso en salares del altiplano andino, norte de Chile. *Andean Geol.* **2019**, *46*, 211–222.
24. Madigan, M.; Bender, K.; Buckley, D.; Sattley, W.M.; Stahl, D. *Brock Biology of Microorganisms*, 15th ed.; Pearson: New York, NY, USA, 2018; 1064p.
25. Thompson, J.B.; Ferris, F.G. Cyanobacterial precipitation of gypsum, calcite, and magnesite from natural alkaline lake water. *Geology* **1990**, *18*, 995–998. [[CrossRef](#)]
26. Demergasso, C.; Chong, G.; Escudero, L.; Pueyo, J.J.; Pedrós-Alió, C. Microbial Precipitation of Arsenic Sulfides in Andean Salt Flats. *Geomicrobiol. J.* **2007**, *24*, 111–123. [[CrossRef](#)]
27. Sánchez-Román, M.; Vasconcelos, C.; Warthmann, R.; Rivadeneyra, M.; McKenzie, J.A. Microbial dolomite precipitation under aerobic conditions: Results from Brejo do Espinho Lagoon (Brazil) and culture experiments. *Int. Assoc. Sedimentol. Spec. Publ.* **2009**, *41*, 167–178.
28. Glunk, C.; Dupraz, C.; Braissant, O.; Gallagher, K.L.; Verrecchia, E.P.; Visscher, P.T. Microbially mediated carbonate precipitation in a hypersaline lake, Big Pond (Eleuthera, Bahamas). *Sedimentology* **2011**, *58*, 720–736. [[CrossRef](#)]
29. Gallagher, K.L.; Kading, T.J.; Braissant, O.; Dupraz, C.; Visscher, P.T. Inside the alkalinity engine: The role of electron donors in the organomineralization potential of sulfate-reducing bacteria. *Geobiology* **2012**, *10*, 518–530. [[CrossRef](#)]
30. Sanz-Montero, M.E.; Cabestrero, Ó.; Sánchez-Román, M. Microbial Mg-rich carbonates in an extreme alkaline lake (Las Eras, Central Spain). *Front. Microbiol.* **2019**, *10*, 148. [[CrossRef](#)]
31. Moore, K.R.; Gong, J.; Pajusalu, M.; Skoog, E.J.; Xu, M.; Feliz Soto, T.; Sojo, V.; Matreux, T.; Baldes, M.J.; Braun, D.; et al. A new model for silicification of cyanobacteria in Proterozoic tidal flats. *Geobiology* **2021**, *19*, 438–449. [[CrossRef](#)]
32. Henke, J.M.; Bassler, B.L. Bacterial social engagements. *Trends Cell Biol.* **2004**, *14*, 648–656. [[CrossRef](#)]
33. Bassler, B.L.; Losick, R. Bacterially speaking. *Cell* **2006**, *125*, 237–246. [[CrossRef](#)]
34. Balows, A.; Trüper, H.G.; Dworkin, M.; Harder, W.; Schleifer, K.H. (Eds.) *The Prokaryotes: A Handbook on the Biology of Bacteria: Ecophysiology, Isolation, Identification, Applications*; Springer Science + Business Media: Berlin/Heidelberg, Germany, 2013.
35. Risacher, F.; Alonso, H.; Salazar, C. The origin of brines and salts in Chilean salars: A hydrochemical review. *Earth-Sci. Rev.* **2003**, *63*, 249–293. [[CrossRef](#)]
36. Hinman, N.W.; Cabrol, N.A.; Gulick, V.; Warren-Rhodes, K.; Tebes, C.; Chong, G.; Demergasso, C. Initial Investigations of Endoevaporitic Gypsum Habitats of Salar de Pajonales, Chile. In *Astrobiology Science Conference, Mesa, AZ (Lunar and Planetary Institute, 2017), Arizona. Abstract; 2017; Volume 3568*, Available online: <https://www.hou.usra.edu/meetings/abscicon2017/eposter/3568.pdf> (accessed on 14 May 2022).
37. Chong Díaz, G.; Demergasso, C.; Urrutia Meza, J.; Vargas, M. El Dominio Salino del Norte de Chile y sus Yacimientos de Minerales Industriales. *Bol. Soc. Geol. Mex.* **2020**, *72*, 00018. [[CrossRef](#)]
38. Pueyo, J.; Demergasso, C.; Escudero, L.; Chong, G.; Cortéz-Rivera, P.; Sanjurjo-Sánchez, J.; Carmona, V.; Giral, S. On the origin of saline compounds in acidic salt flats (Central Andean Altiplano). *Chem. Geol.* **2021**, *574*, 120155. [[CrossRef](#)]
39. Naranjo, J.A.; Villa, V.; Venegas, C. Geología de las áreas Salar de Pajonales y Cerro Moño, regiones de Antofagasta y Atacama. *Serv. Nac. Geol. Min. Carta Geol. Chile Ser. Geol. Básica* **2013**, *153–154*, 1.
40. Rodríguez, C. *Geología del Salar Pajonales (7209000-7226500N 510000-530 000E) y Antecedentes de su Microbiota, Antofagasta, Norte de Chile*; Memoria Para Optar al Título de Geólogo; Universidad Católica del Norte: Antofagasta, Chile, 2018; 104p.
41. Benison, K.C. The physical and chemical sedimentology of two high-altitude acid salars in Chile: Sedimentary processes in an extreme environment. *J. Sediment. Res.* **2019**, *89*, 147–167. [[CrossRef](#)]
42. Dunai, T.J.; López, G.A.G.; Juez-Larré, J. Oligocene–Miocene age of aridity in the Atacama Desert revealed by exposure dating of erosion-sensitive landforms. *Geology* **2005**, *33*, 321–324. [[CrossRef](#)]
43. Kampf, S.K.; Tyler, S.W. Spatial characterization of land surface energy fluxes and uncertainty estimation at the Salar de Atacama, Northern Chile. *Adv. Water Resour.* **2006**, *29*, 336–354. [[CrossRef](#)]
44. Schween, J.H.; Hoffmeister, D.; Löhnert, U. Filling the observational gap in the Atacama Desert with a new network of climate stations. *Glob. Planet. Change* **2020**, *184*, 103034. [[CrossRef](#)]
45. Duffie, J.A.; Beckman, W.A. Solar Radiation. In *Solar Engineering of Thermal Processes*, 4th ed.; Wiley: Hoboken, NJ, USA, 2013; pp. 12–20.
46. Bozkurt, D.; Rondanelli, R.; Garreaud, R.; Arriagada, A. Impact of Warmer Eastern Tropical Pacific SST on the March 2015 Atacama Floods. *Mon. Weather Rev.* **2016**, *144*, 4441–4460. [[CrossRef](#)]
47. Cabré, A.; Remy, D.; Aguilar, G.; Carretier, S.; Riquelme, R. Mapping rainstorm erosion associated with an individual storm from InSAR coherence loss validated by field evidence for the Atacama Desert. *Earth Surf. Processes Landf.* **2020**, *45*, 2091–2106. [[CrossRef](#)]

48. Hinman, N.W.; Hofmann, M.H.; Warren-Rhodes, K.; Phillips, M.; Nofke, N.; Cabrol, N.A.; Chong-Diaz, G.; Demergasso, C.; Tebes Cayo, C.; Cabestrero, Ó.; et al. Surface Morphologies in a Mars-analog Ca-sulfate Salar, High Andes, Northern Chile. *Front. Astron. Space Sci.* **2022**, *8*, 235. [[CrossRef](#)]
49. Phillips, M.S.; Moersch, J.E.; Cabrol, N.A.; Candela, A.; Wettergreen, D.; Warren-Rhodes, K.; Hinman, N.W.; Rhodes, R.; Team, T.S.I.N. Mapping planetary features from ground to orbit with Deep Learning: Application to habitats in a Mars-analog environment. *Astrobiology* **2022**. *Submitted*.
50. Escudero, L.W.; Bijman, J.; Chong, G.; Pueyo, J.J.; Demergasso, C. Geochemistry and microbiology in an acidic high altitude (4000 m) salt flat, high Andes, Northern Chile. *Adv. Mater. Res.* **2013**, *825*, 28–32. [[CrossRef](#)]
51. Escudero, L.W.; Oetiker, N.; Gallardo, K.; Tebes-Cayo, C.; Guajardo, M.; Núñez, C.; Davis-Belmar, C.; Pueyo, J.J.; Chong, G.; Demergasso, C. A thiotrophic microbial community in an acidic brine lake in Northern Chile. *Antonie Leeuwenhoek* **2018**, *111*, 1403–1419. [[CrossRef](#)] [[PubMed](#)]
52. Tebes-Cayo, C.; Rodriguez, C.; Demergasso, C.; Chong, G.; Parro, V.; Sánchez-García, L.; Carrizo, D.; Hinman, N.W.; Warren-Rhodes, K.; Cabrol, N.A. Microbial Participation on the Formation and the Preservation of Gypsum Structures from Salar de Pajonales, Northern of Chile. In *2019 Astrobiology Science Conference*; AGU: Washington, DC, USA, 2019; Available online: https://agu.confex.com/data/extendedabstract/agu/abscon19/Paper_482718_extendedabstract_31733_0.pdf (accessed on 14 May 2022).
53. Tebes-Cayo, C.; Demergasso, C.; Chong, G.; Cabestrero, Ó.; Sanz-Montero, M.E.; Castro-Nallar, E.; Cabrol, N. Geochemistry and microbial communities in Salar de Pajonales and Salar de Gorbea, Northern Chile: Influence on the gypsum microbialites formation. *Geotemas* **2021**, *18*, 458–462.
54. Otálora, F.; Criado-Reyes, J.; Baselga, M.; Canals, A.; Verdugo-Escamilla, C.; García Ruiz, J.M. Hydrochemical and mineralogical evolution through evaporitic processes in Salar de Llamara Brines (Atacama, Chile). *ACS Earth Space Chem.* **2020**, *4*, 882–896. [[CrossRef](#)]
55. Reid, R.P.; Oehlert, A.M.; Suosaari, E.P.; Demergasso, C.; Chong, G.; Escudero, L.V.; Piggot, A.M.; Lascu, I.; Palma, A.T. Electrical conductivity as a driver of biological and geological spatial heterogeneity in the Puquios, Salar de Llamara, Atacama Desert, Chile. *Sci. Rep.* **2021**, *11*, 12769. [[CrossRef](#)] [[PubMed](#)]
56. Urrutia, J.; Jodar, J.; Medina, A.; Herrera, C.; Chong, G.; Urqueta, H.; Luque, J.A. Hydrogeology and sustainable future groundwater abstraction from the Agua Verde aquifer in the Atacama Desert, northern Chile. *Hydrogeol. J.* **2018**, *26*, 1989–2007. [[CrossRef](#)]
57. Benison, K.C.; Karmanocky, F.J., III. Could microorganisms be preserved in Mars gypsum? Insights from terrestrial examples. *Geology* **2014**, *42*, 615–618. [[CrossRef](#)]
58. Parkhurst, D.L.; Appelo, C.A.J. Description of Input and Examples for PHREEQC Version 3: A Computer Program for Speciation, Batch-Reaction, One-Dimensional Transport, and Inverse Geochemical Calculations; U.S. Geological Survey Techniques and Methods, No. 6-A43. 2013. Available online: <http://pubs.usgs.gov/tm/06/a43> (accessed on 14 May 2022).
59. Pitzer, K.S. Thermodynamics of electrolytes. I. Theoretical basis and general equations. *J. Phys. Chem.* **1973**, *77*, 268–277. [[CrossRef](#)]
60. Castenholz, R.W. Phylum BX Cyanobacteria. Oxygenic photosynthetic bacteria. In *Bergey's Manual of Systematic Bacteriology*; Boone, D.R., Castenholz, R.W., Garrity, G.M., Eds.; The Archea and Deeply Branching and Photrophic Bacteria; Springer: New York, NY, USA, 2001; Volume 1, pp. 473–599.
61. Díaz, C.; Maidana, N. *Diatomeas de los Salares de Atacama y Punta Negra II Región*; Centro de Ecología Aplicada: La Reina, Chile, 2005.
62. Silverstone, S.; Nelson, M.; Alling, A.; Allen, J.P. Soil and crop management experiments in the Laboratory Biosphere: An analogue system for the Mars on Earth[®] facility. *Adv. Space Res.* **2005**, *35*, 1544–1551. [[CrossRef](#)]
63. Cockell, C.S.; Santomartino, R.; Finster, K.; Waajen, A.C.; Eades, L.J.; Moeller, R.; Rettberg, P.; Fuchs, F.M.; Van Houdt, R.; Leys, N.; et al. Space station biomineral experiment demonstrates rare earth element extraction in microgravity and Mars gravity. *Nat. Commun.* **2020**, *11*, 5523. [[CrossRef](#)]
64. Graue, J.; Engelen, B.; Cypionka, H. Degradation of cyanobacterial biomass in anoxic tidal-flat sediments: A microcosm study of metabolic processes and community changes. *ISME J.* **2012**, *6*, 660–669. [[CrossRef](#)]
65. García-Maldonado, J.Q.; Escobar-Zepeda, A.; Raggi, L.; Bebout, B.M.; Sanchez-Flores, A.; López-Cortés, A. Bacterial and archaeal profiling of hypersaline microbial mats and endoevaporites, under natural conditions and methanogenic microcosm experiments. *Extremophiles* **2018**, *22*, 903–916. [[CrossRef](#)] [[PubMed](#)]
66. Llorós, M.; Gaju, N.; de Oteyza, T.G.; Grimalt, J.O.; Esteve, I.; Martínez-Alonso, M. Microcosm experiments of oil degradation by microbial mats. II. The changes in microbial species. *Sci. Total Environ.* **2008**, *393*, 39–49. [[CrossRef](#)] [[PubMed](#)]
67. Bebout, B.M.; Carpenter, S.P.; Des Marais, D.J.; Discipulo, M.; Embaye, T.; Garcia-Pichel, F.; Hoehler, T.M.; Hogan, M.; Jahnke, L.L.; Keller, R.M.; et al. Long-term manipulations of intact microbial mat communities in a greenhouse laboratory: Simulating earth's present and past field environments. *Astrobiology* **2002**, *2*, 383–402. [[CrossRef](#)] [[PubMed](#)]
68. Kawaguchi, T.; Decho, A.W. Isolation and biochemical characterization of extracellular polymeric secretions (EPS) from modern soft marine stromatolites (Bahamas) and its inhibitory effect on CaCO₃ precipitation. *Prep. Biochem. Biotechnol.* **2002**, *32*, 51–63. [[CrossRef](#)] [[PubMed](#)]
69. McLoughlin, N.; Wilson, L.A.; Brasier, M.D. Growth of synthetic stromatolites and wrinkle structures in the absence of microbes—implications for the early fossil record. *Geobiology* **2008**, *6*, 95–105. [[CrossRef](#)] [[PubMed](#)]

70. Couradeau, E.; Benzerara, K.; Moreira, D.; Gerard, E.; Kaźmierczak, J.; Tavera, R.; López-García, P. Prokaryotic and eukaryotic community structure in field and cultured microbialites from the alkaline Lake Alchichica (Mexico). *PLoS ONE* **2011**, *6*, e28767. [[CrossRef](#)]
71. Newman, S.A.; Mariotti, G.; Pruss, S.; Bosak, T. Insights into cyanobacterial fossilization in Ediacaran siliciclastic environments. *Geology* **2016**, *44*, 579–582. [[CrossRef](#)]
72. Newman, S.A.; Klepac-Ceraj, V.; Mariotti, G.; Pruss, S.B.; Watson, N.; Bosak, T. Experimental fossilization of mat-forming cyanobacteria in coarse-grained siliciclastic sediments. *Geobiology* **2017**, *15*, 484–498. [[CrossRef](#)]
73. Osman, J.R.; Viedma, P.; Mendoza, J.; Cotoras, D. Bacterial and Geochemical Composition of Thrombolites from Lake Sarmiento, Torres del Paine National Park of Chilean Patagonia. *Geomicrobiol. J.* **2020**, *37*, 376–388. [[CrossRef](#)]
74. Osman, J.R.; Viedma, P.; Mendoza, J.; Fernandes, G.; DuBow, M.S.; Cotoras, D. Prokaryotic diversity and biogeochemical characteristics of field living and laboratory cultured stromatolites from the hypersaline Laguna Interna, Salar de Atacama (Chile). *Extremophiles* **2021**, *25*, 327–342. [[CrossRef](#)]
75. Baker, M. 1500 scientists lift the lid on reproducibility. *Nat. News* **2016**, *533*, 452. [[CrossRef](#)] [[PubMed](#)]
76. Cabestrero, Ó.; Sanz-Montero, M.E.; del Buey, P.; Tebes-Cayo, C.; Demergasso, C.; Visscher, P.T. Experiments with microbial mats from shallow lakes: Metabolic influence of the microorganisms in the precipitation of minerals. *Geotemas* **2021**, *18*, 144–146.
77. Marín, S.; Cabestrero, O.; Demergasso, C.; Olivares, S.; Zetola, V.; Vera, M. An indigenous bacterium with enhanced performance of microbially-induced Ca-carbonate biomineralization under extreme alkaline conditions for concrete and soil-improvement industries. *Acta Biomater.* **2021**, *120*, 304–317. [[CrossRef](#)] [[PubMed](#)]
78. Popall, R.M.; Bolhuis, H.; Muyzer, G.; Sánchez-Román, M. Stromatolites as biosignatures of atmospheric oxygenation: Carbonate biomineralization and UV-C resilience in a *Geitlerinema* sp.-dominated culture. *Front. Microbiol.* **2020**, *11*, 948. [[CrossRef](#)]
79. Mellage, A.; Smeaton, C.M.; Furman, A.; Atekwana, E.A.; Rezanezhad, F.; Van Cappellen, P. Linking spectral induced polarization (SIP) and subsurface microbial processes: Results from sand column incubation experiments. *Environ. Sci. Technol.* **2018**, *52*, 2081–2090. [[CrossRef](#)]
80. Duteil, T.; Bourillot, R.; Grégoire, B.; Virolle, M.; Brigaud, B.; Nouet, J.; Braissant, O.; Portier, E.; Féliès, H.; Patrier, P.; et al. Experimental formation of clay-coated sand grains using diatom biofilm exopolymers. *Geology* **2020**, *48*, 1012–1017. [[CrossRef](#)]
81. Moore, K.R.; Pajusalu, M.; Gong, J.; Sojo, V.; Matreux, T.; Braun, D.; Bosak, T. Biologically mediated silicification of marine cyanobacteria and implications for the Proterozoic fossil record. *Geology* **2020**, *48*, 862–866. [[CrossRef](#)]
82. Brehm, U.; Gorbushina, A.; Mottershead, D. The role of microorganisms and biofilms in the breakdown and dissolution of quartz and glass. In *Geobiology: Objectives, Concepts, Perspectives*; Elsevier: Amsterdam, The Netherlands, 2005; pp. 117–129.
83. Palm, A. The Dissolution of Diatoms in Marine Microbial Mats. Master's Thesis, University of Connecticut, Storrs, CT, USA, 2018; 92p. Available online: https://opencommons.uconn.edu/gs_theses/1219 (accessed on 14 May 2022).
84. Fecskeová, L.K.; Piwosz, K.; Hanusová, M.; Nedoma, J.; Znachor, P.; Koblížek, M. Diel changes and diversity of pufM expression in freshwater communities of anoxygenic phototrophic bacteria. *Sci. Rep.* **2019**, *9*, 1–12. [[CrossRef](#)]
85. Guerrero, M.C.; Tadeo, A.B.; de Wit, R. Environmental factors controlling the development of microbial mats in inland saline lakes; the granulometric composition of the sediment. In *Microbial Mats*; Springer: Berlin/Heidelberg, Germany, 1994; pp. 85–90.
86. Prisciandaro, M.; Lancia, A.; Musmarra, D. The retarding effect of citric acid on calcium sulfate nucleation kinetics. *Ind. Eng. Chem. Res.* **2003**, *42*, 6647–6652. [[CrossRef](#)]
87. Rabizadeh, T.; Peacock, C.L.; Benning, L.G. Carboxylic acids: Effective inhibitors for calcium sulfate precipitation? *Mineral. Mag.* **2014**, *78*, 1465–1472. [[CrossRef](#)]
88. Ossorio, M.; Stawski, T.M.; Rodríguez-Blanco, J.D.; Sleutel, M.; García-Ruiz, J.M.; Benning, L.G.; Van Driessche, A.E. Physico-chemical and additive controls on the multistep precipitation pathway of gypsum. *Minerals* **2017**, *7*, 140. [[CrossRef](#)]
89. Nicoleau, L.; Van Driessche, A.E.; Kellermeier, M. A kinetic analysis of the role of polymers in mineral nucleation. The example of gypsum. *Cem. Concr. Res.* **2019**, *124*, 105837. [[CrossRef](#)]
90. Sangwal, K. *Additives and Crystallization Processes: From Fundamentals to Applications*; John Wiley & Sons: Hoboken, NJ, USA, 2007.
91. Amjad, Z.; Demadis, K.D. (Eds.) *Mineral Scales and Deposits: Scientific and Technological Approaches*; Elsevier: Amsterdam, The Netherlands, 2015.
92. Dupraz, C.; Reid, R.P.; Braissant, O.; Decho, A.W.; Norman, R.S.; Visscher, P.T. Processes of carbonate precipitation in modern microbial mats. *Earth-Sci. Rev.* **2009**, *96*, 141–162. [[CrossRef](#)]
93. Douglas, T.; Mann, S. Oriented nucleation of gypsum (CaSO₄·2H₂O) under compressed Langmuir monolayers. *Mater. Sci. Eng. C* **1994**, *1*, 193–199. [[CrossRef](#)]
94. Wang, J.; Wang, L.; Miao, R.; Lv, Y.; Wang, X.; Meng, X.; Yang, R.; Zhang, X. Enhanced gypsum scaling by organic fouling layer on nanofiltration membrane: Characteristics and mechanisms. *Water Res.* **2016**, *91*, 203–213. [[CrossRef](#)] [[PubMed](#)]
95. Wierchos, J.; Casero, M.C.; Artieda, O.; Ascaso, C. Endolithic microbial habitats as refuges for life in polyextreme environment of the Atacama Desert. *Curr. Opin. Microbiol.* **2018**, *43*, 124–131. [[CrossRef](#)] [[PubMed](#)]
96. Van den Heuvel, D.B. Precipitation Pathways of Amorphous Silica. Ph.D. Thesis, University of Leeds, Leeds, UK, 2016; 241p.
97. Daza Brunet, R. Distribución, Composición y Génesis (Biótica/Abiótica) de los Espeleotemas de las Cuevas Volcánicas de la Isla Terceira (Azores, Portugal). Ph.D. Thesis, Complutense University of Madrid, Madrid, Spain, 2015; 178p.
98. van den Heuvel, D.B.; Stawski, T.M.; Tobler, D.J.; Wirth, R.; Peacock, C.L.; Benning, L.G. Formation of silica-lysozyme composites through co-Precipitation and adsorption. *Front. Mater.* **2018**, *5*, 19. [[CrossRef](#)]

99. Konhauser, K.O. *Introduction to Geomicrobiology*; Blackwell Science Ltd.: Oxford, UK, 2007; 452p.
100. Paerl, H.W.; Steppe, T.F.; Reid, R.P. Bacterially mediated precipitation in marine stromatolites. *Environ. Microbiol.* **2001**, *3*, 123–130. [[CrossRef](#)]
101. Pozo, M.; Calvo, J.P. An overview of authigenic magnesian clays. *Minerals* **2018**, *8*, 520. [[CrossRef](#)]
102. Martín-Pérez, A.; La Iglesia, Á.; Almendros, G.; González-Pérez, J.A.; Alonso-Zarza, A.M. Precipitation of kerolite and sepiolite associated with Mg-rich carbonates in a cave environment. *Sediment. Geol.* **2021**, *411*, 105793. [[CrossRef](#)]
103. Cortez, P. *Caracterización Geológica de los Salares Gorbea e Ignorado y su Asociación con su Microbiota*; Universidad Católica del Norte: Antofagasta, Chile, 2014; 200p.
104. Rouchy, J.M.; Monty, C. Gypsum microbial sediments: Neogene and modern examples. In *Microbial Sediments*; Springer: Berlin/Heidelberg, Germany, 2000; pp. 209–216.
105. Sanz-Montero, M.E.; Rodríguez-Aranda, J.P.; Calvo, J.P. Mediation of endoevaporitic microbial communities in early replacement of gypsum by dolomite: A case study from Miocene Lake deposits of the Madrid Basin, Spain. *J. Sediment. Res.* **2006**, *76*, 1257–1266. [[CrossRef](#)]
106. Sanz-Montero, M.E.; Rodríguez-Aranda, J.P.; del Cura, M.A.G. Bioinduced precipitation of barite and celestite in dolomite microbialites: Examples from Miocene lacustrine sequences in the Madrid and Duero Basins, Spain. *Sediment. Geol.* **2009**, *222*, 138–148. [[CrossRef](#)]
107. Allwood, A.C.; Burch, I.W.; Rouchy, J.M.; Coleman, M. Morphological biosignatures in gypsum: Diverse formation processes of Messinian (~6.0 Ma) gypsum stromatolites. *Astrobiology* **2013**, *13*, 870–886. [[CrossRef](#)] [[PubMed](#)]
108. Manning-Berg, A.R.; Kah, L.C. Proterozoic microbial mats and their constraints on environments of silicification. *Geobiology* **2017**, *15*, 469–483. [[CrossRef](#)] [[PubMed](#)]
109. Manning-Berg, A.R.; Wood, R.S.; Williford, K.H.; Czaja, A.D.; Kah, L.C. The taphonomy of proterozoic microbial mats and implications for early diagenetic silicification. *Geosciences* **2019**, *9*, 40. [[CrossRef](#)]